On Maintaining Bistability of Prestressed Laminates After Clamping

Karthik Boddapati^a, Juan C. Osorio^a, Andres F. Arrieta^{a,*}

^aSchool of Mechanical Engineering, Purdue University, West Lafayette, Indiana, 47907, USA

Abstract

Bistable composite laminates exhibit a high degree of shape change and stiffness variation between their stable configurations, making them suitable for applications in morphing structures and energy harvesting. However, integration of these laminates into larger systems often imposes different boundary conditions, which can eliminate one of their stable states. Moreover, clamping one or more edges of a rectangular bistable laminate causes a drastic change in its strain energy landscape, indicating a strong interplay between the laminate geometry, boundary conditions, and prestress. In this work, we investigate the effect of clamping on the bistability of rectangular prestressed laminates. An analytical approach is proposed to examine the deflection decay imposed by the boundary condition along the laminate's length. Different prestress values, laminate dimensions, and material properties are analyzed to establish their effect on the curvature change due to the localized clamp effect. A length criterion is determined to guarantee bistability after clamping the bistable laminate, suggesting the need to utilize complementary techniques to retain the bistable behavior for orthotropic prestressed laminates. Different strategies to counter the clamped edge effect and thereby retain the bistability of these types of laminates are then examined. The proposed analytical model is expanded to consider multi-section composite laminates, showing the role of the symmetric regions in bistability retention. Finally, the results from the model are validated against experiments.

Keywords: bistability, prestressed laminates, clamped boundary condition, curvature decay, transition region

Nomenclature

 L_x = x direction or longitudinal dimension of the laminate L_y = y direction or transverse dimension of the laminate

AR = aspect ratio of the laminate

R = radius of curvature t = laminate thickness

 σ, ε = in-plane stress and strain vectors κ = vector of mid-plane curvatures

 L_p = ploy length

Email address: aarrieta@purdue.edu (Andres F. Arrieta)

^{*}Corresponding author

 M^{ps} = residual internal bending moment due to prestress

 $E, G, \beta, \nu = \text{Young's modulus, shear modulus, modular ratio, Poisson's ratio}$

 \mathbb{Q} = reduced stiffness matrix $\mathbb{A}, \mathbb{B}, \mathbb{D}$ = material stiffness matrices

 n_{ply} = number of plies in the composite layup χ = vector of mid-plane curvature changes

k = decay parameter U = strain energy density

 \bar{U} = strain energy

 L_s = prestress-free transition zone length

TR = transition zone ratio

 L_i = interface region boundary location

 u^i, v^i = in-plane displacement fields in x and y directions w^i = out-of-plane displacement field in z direction c^i_{pqr} = coefficient of $x^q y^r$ term in the displacement fields N_T, M_T = thermal stress and moment resultant matrices

 W_{ext} = work due to external loading

 U_{lam} = total potential energy VS = variable stiffness BC = boundary condition FEA = finite element analysis CLT = classical lamination theory

DOF = degree of freedom

1. Introduction

Bistable composite laminates have received significant attention for morphing and shape-shifting applications [1-6], owing to their intrinsic ability to deflect between stable shapes and their inherent stiffness. In this regard, bistable laminates serve as a unique solution, offering the possibility to program multiple stable shapes and stiffness adaptation in the structural system with minimal actuation [7, 8]. Several works have introduced and analyzed these types of laminates using different analytical, semi-analytical, numerical, and experimental procedures. Hyer [1] discovered the existence of two room temperature cylindrical shapes in unsymmetric cross-ply laminates and calculated them using the Rayleigh-Ritz energy minimization approach while accounting for geometric nonlinearities [9, 10]. Hyer's work was later extended to include anti-symmetric angle-ply laminates, which also exhibited bistable behavior, but the room temperature shapes were no longer cylindrical [2, 11, 12]. Iqbal and Pellegrino [13] studied bistable composite shells for deployable structures. These composites had anti-symmetric layups and were cured with an initial curvature to exhibit an extended state and a compact rolled-up state similar to a tape measure, both of which were cylindrical in nature. These kinds of asymmetric bistable composite shells have become increasingly popular for applications including composite slit tubes [14–16], composite tape springs [17–19], and deployable composite booms [20–22]. Consequently, analytical models for multistable plates [23–26] and shells [27–29] have been developed to predict their stable configurations and analyze the localized deformations and curvatures. Advances have also been made in altering the stacking sequence of bistable composites

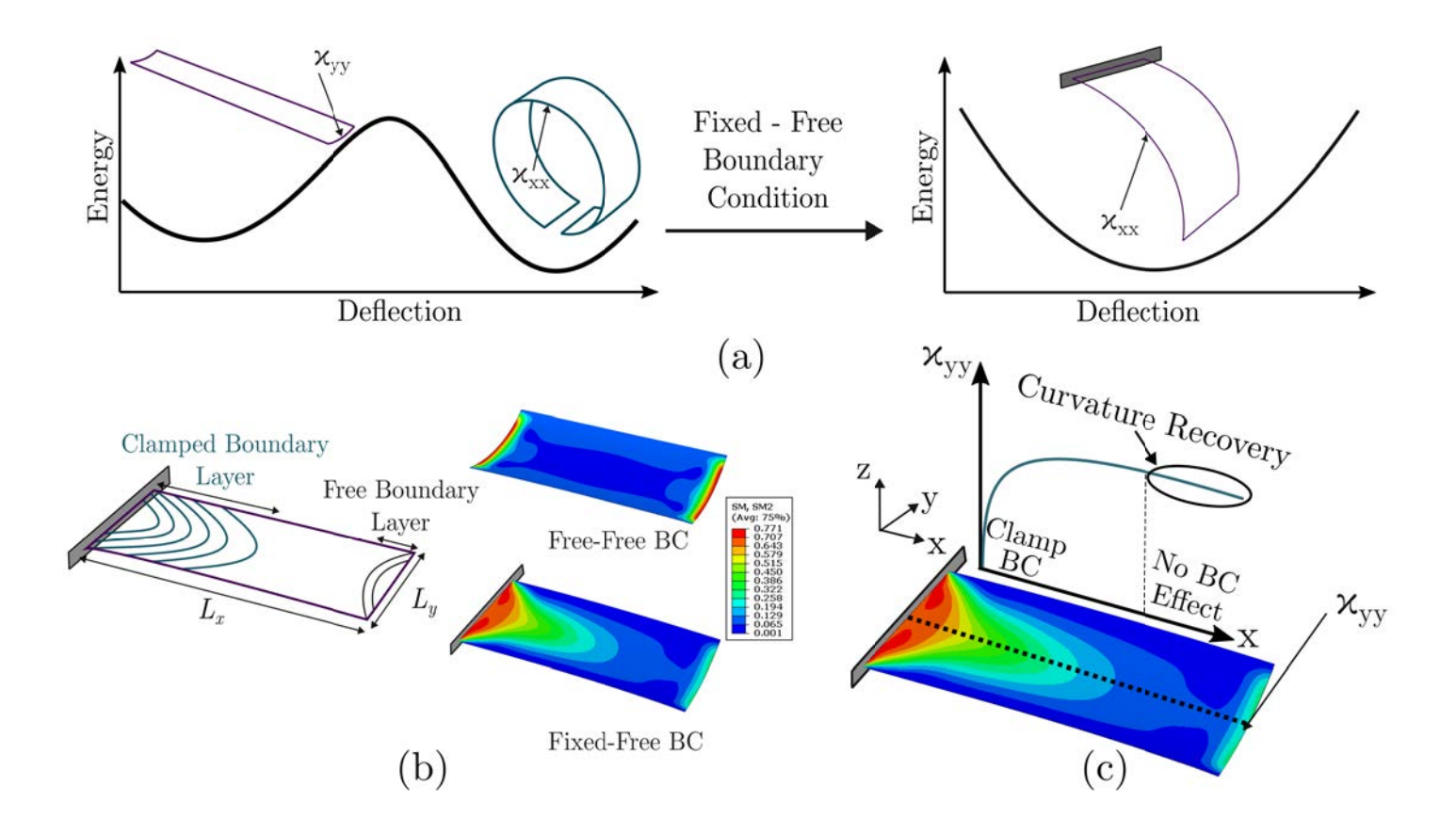


Figure 1: Effect of boundary conditions on the bistable behavior of prestressed laminates. (a) Fixed boundary condition effect on the energy landscape of prestressed bistable laminates. (b) Boundary layer effect on the prestressed laminate (numerical model observation). (c) Variation from imposing the clamped boundary condition in the y directional curvature along the x-axis showing the recovery of initial transverse curvature along the laminate's length.

to enable multistability and enhance their stiffness properties. Bistable hybrid symmetric laminates were presented in Ref. [30] with the ability to exhibit two stable configurations having identical curvatures with opposite signs. Several works have focused on the modeling and analysis of unsymmetric variable stiffness (VS) bistable laminates with curvilinear fiber paths to tailor their snap-through loads [31, 32]. Recently, Zhang et al. [33] incorporated transition elements with anti-symmetric layups into composite laminates to demonstrate multistable structures with up to 16 stable states, thereby increasing the degree of design freedom for morphing structures.

In recent years, considerable attention has been dedicated to assessing the mechanical behavior of these structures as a function of their geometry, layup, prestress, and imposing different boundary conditions [34–39]. Different systems have been proposed to leverage their geometry and stiffness change for aircraft morphing applications. Daynes et al. [5] designed a bistable trailing edge flap to adapt between hover and forward flight. The stiffness characteristics for asymmetric bistable laminates were optimized for decreased deflection under loading by Betts et al. [40]. Arrieta et al. investigated and modeled the response of wing-shaped bistable laminates under aerodynamic response [41, 42] and proposed configurations for passive load alleviation [43, 44]. Kuder et al. [45] studied the aero-structural response of variable stiffness

bistable laminates and optimized their location and properties to maximize the compliance selectivity when embedded into airfoils. Scarselli et al. [36] characterized the highly nonlinear behavior dependence of bistable composites on stress-strain trends and potential energy. More recently, Boddapati et al. [46] conceptualized a low aspect ratio slitted bistable laminate and demonstrated its capability as an effective trailing edge morphing device using wind tunnel experiments [47].

However, one of the main challenges of multistable composites arises from the loss of one or more of their stable states once they are integrated into a larger system [48]. Despite the structure's versatility, bistability can be highly affected by the imposed boundary conditions (BCs) during coupling [49] (see Fig. 1a). These effects should be considered when designing, optimizing, and manufacturing bistable composites to ensure that all their unique characteristics are retained once coupled to the complete system. Different studies have focused on the effect of boundary conditions on curved laminates [25, 50, 51]. Barois et al. [52] examined the effect of a curved edge along the length of an elastic strip to establish the critical length at which the boundary condition effect decays. Bistable orthotropic tape springs were analyzed for their stiffness and strains in different shapes, and their ploy size and length in Refs. [38, 53]. Brunetti et al. [50] used semi-analytical approaches and simplified models [37] to examine the effect of initial laminate curvature and composite layup on the loss of bistability and boundary layer effect produced by fixed boundary conditions. While their approaches describe the main implications of localized effects of boundary conditions and their impact on curvature, a criterion to guarantee bistability after clamping has not yet been established. Although the discussed models are able to accurately calculate the stable shapes of bistable laminates, there has been no work toward analyzing the loss of bistability due to BCs from an analytical perspective to the best of the authors' knowledge.

This work focuses on understanding the role of a clamped BC on the loss of bistability of orthotropic prestressed laminates. We start our analysis by only considering cross-ply laminates that are bistable when all of their edges are free (free-free condition, see Fig. 1a) and the impact on their stability after imposing a clamped boundary condition on one of the edges (fixed-free condition). A loss of bistability is observed due to the boundary condition and its propagation over the laminate domain rationalized as a result of Saint-Venant's end effect. To further examine this phenomenon and the effect of the boundary condition, we consider the clamped edge effect as a boundary layer (see Fig. 1b) that exponentially decays over the length of the domain. By making this assumption, the full length of the affected region can be examined [54, 55], and criteria can be determined for which the initial curvature of the laminate is no longer affected by the localized boundary condition effects (see Fig. 1c). We establish an analytical model to capture the decay length and change in curvature along the longitudinal axis of the laminate as a function of the initial curvature, geometry, and prestress of the laminate. The analytical model allows for determining the length at which the curvature is fully recovered, thereby yielding criteria to guarantee bistability after the structure is clamped.

This paper is organized as follows. In section 2, the initial geometry for an orthotropic bistable prestressed laminate is given. In addition, material properties, prestress conditions, and the two stable states for the free-free boundary condition are shown. Section 3 shows the extensible shell model to capture the curvature and stress decay generated by boundary conditions and propagated along the domain. Section 4 analyzes the decay predicted by the model and establishes the effect of the boundary condition on the loss of bistability. Additionally, validation with the finite element analysis (FEA) for different isotropic and orthotropic cases is performed and analyzed. A strategy to retain bistability in the orthotropic case is discussed in section 5, and the model is extended to account for these strategies. Finally, the results

Table 1: Material properties of Grafil TR50S/Newport 301 unidirectional pre-preg.

E_{11} (GPa)	E_{22} (GPa)	G_{12} (GPa)	ν_{12}	$\alpha_{11} \ (^{\circ}\mathrm{C}^{-1})$	$\alpha_{22} \; (^{\circ}\mathrm{C}^{-1})$	$\rho \; (\mathrm{kgm}^{-3})$	$t_{ply} \text{ (mm)}$
140	9.4	5	0.3	-1.79E - 08	2.15E - 05	1346	0.12

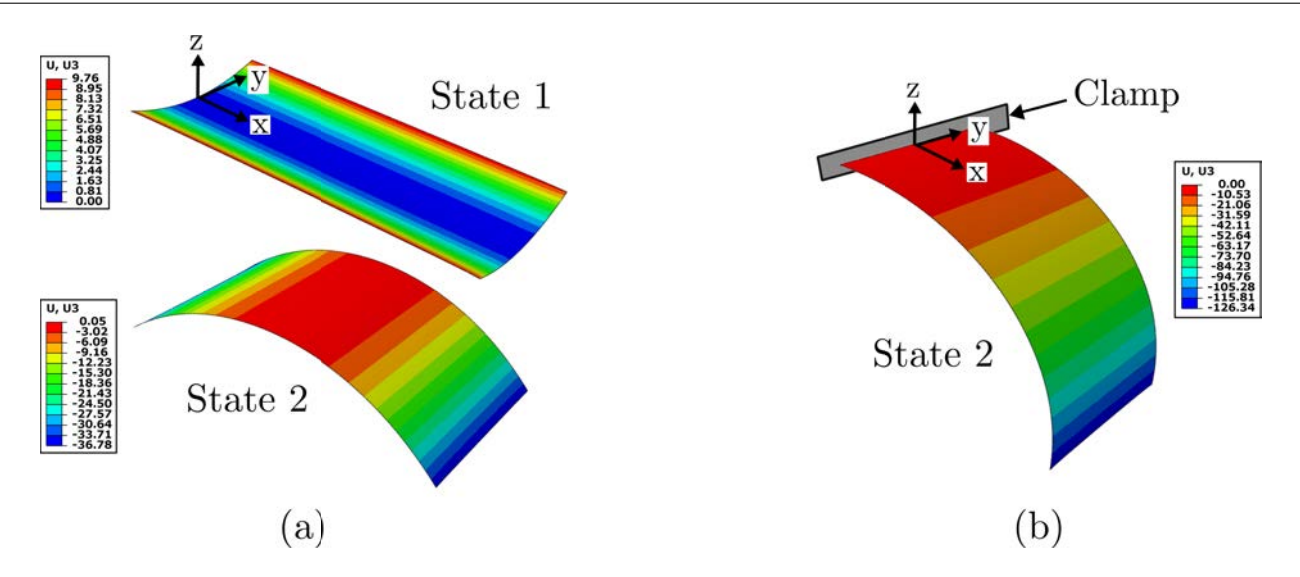


Figure 2: Effect of the clamped boundary condition on the bistability of a rectangular composite laminate. (a) State 1 and State 2 of a free-free laminate with AR = 2. (b) Loss of state 1 by clamping the laminate's edge.

from the model are compared against experiments in section 6.

2. Orthotropic bistable laminates

We consider a rectangular composite laminate with $L_x = 200$ mm, $L_y = 100$ mm, a $[90/0]_T$ layup, and material properties as listed in Table 1 to demonstrate the effect of altering the geometry and boundary conditions on its bistability using FEA in ABAQUS®. The Abaqus/Standard module is employed for the numerical analysis. The laminate was meshed using four-node, doubly curved, reduced integration, S4R linear shell elements with an element size of 2 mm. The nonlinear geometry (NLgeom) solver is turned on to account for the large out-of-plane deflections and snap-through instabilities. Artificial damping in the order of 10^{-7} is added to enable convergence [56]. The aspect ratio of the laminate is defined as follows:

$$AR = \frac{L_x}{L_y}. (1)$$

Upon cooling from the curing temperature (130°C) to room temperature (20°C), the laminate undergoes a temperature change of $\Delta T = -110$ °C developing a curvature to relieve the incompatibility arising from the unsymmetric lamination and the imposed thermal prestrain ($\alpha \Delta T$), where α is the thermal expansion coefficient. In the finite element model, this negative temperature change is imposed as an initial predefined temperature field of 110°C to the entire laminate and modified to 0°C in the subsequent step. The adopted

curvature is associated with one of the stable states of the laminate. For the geometry and material properties given, the two stable states of the laminate obtained from FEA are shown in Fig. 2a. For a $[90/0]_T$ stacking sequence, states 1 and 2 are almost perfectly cylindrical with non-zero curvatures in the y and x directions, respectively, while their curvatures in the respective orthogonal directions are negligible. Although asymmetric bistable laminates are known to display anticlastic curvatures close to the edges [26, 57, 58], this behavior is not very pronounced for geometries similar to the ones we analyze [59] and is therefore ignored in this study. With the center point of the laminate fixed, its four corners are subjected to out-of-plane (z) displacement boundary conditions to switch from one stable state to another. Upon clamping the shorter edge, the laminate only exhibits state 2, therefore losing its bistable behavior, as shown in Fig. 2b. The clamp is replicated using the ENCASTRE boundary condition in ABAQUS[®].

3. Extensible shell model for clamped laminates

As seen in Fig. 2a, state 2 of the laminate remains stable irrespective of the edge being clamped, while state 1 is lost after clamping. Understanding the behavior of state 1 under a clamped BC would shed light on the cause of bistability loss. To this end, we employ a model inspired by prior efforts by Seffen et al. [38] to predict the curvature of thin shells with an initial shape similar to the laminate in state 1 after a clamped BC is imposed. This model was originally developed to predict the "ploy length" (L_p) in Fig. 3) of folded orthotropic tape springs. A folded tape spring exhibits a zero transverse curvature at the central fold and a non-zero transverse curvature of 1/R at the end of the ploy region (see Fig. 3a), where R is its initial transverse radius of curvature. State 1 of the laminate can be treated as a thin shell, which typically exhibits t/R < 1/20 [60], where t is the uniform shell thickness. Similar to a tape spring, state 1 has an initial transverse curvature of $\kappa_{yy}^0 = 1/R$, while its longitudinal curvature is $\kappa_{xx}^0 = 0$, as shown in Fig. 3b (top). Upon clamping the edge at x=0, $\kappa_{yy}(x=0)=0$ and its value increases over the length of the laminate eventually recovering its initial non-zero curvature, which is also accompanied by a change in its longitudinal curvature. This behavior is schematically shown in Fig. 3b (bottom). The length of the laminate, L_p , at which the initial transverse curvature is recovered $(\kappa_{yy}(x=L_p)=1/R)$ is defined as the ploy length in our case. One main difference between the tape spring studied in Ref. [38] and our model for bistable laminates is that the tape spring is initially in a stress-free state, while the laminates attain their transverse curvature in state 1 due to the induced thermal prestress while curing. This prestress appears as an internal residual moment in the x direction, M_{xx}^{ps} , when the laminate is in state 1, and as a residual moment in the y direction, M_{yy}^{ps} , when the laminate is in state 2 [61]. M_{xx}^{ps} and M_{yy}^{ps} have similar magnitudes but opposite signs when all edges are free. Both of these residual moments affect the energy landscape of the laminate under deformation and therefore have an effect on the laminate's behavior when clamped. Another difference is that the tape springs studied in [38] have completely decoupled bending and stretching behaviors, while the $[90/0]_T$ stacking sequence of the bistable laminates induces a coupling between their bending and extensional deformations [62]. The model we propose below takes into account these two major differences, thereby extending the capabilities of the prior work to include prestressed shells with bending-stretching coupling.

3.1. Material stiffness matrices

We consider shell geometries with $t \ll L_y \ll L_x$ and an initial transverse curvature of 1/R. This state is considered to be stress-free, and the prestress terms will be added later in the form of residual bending

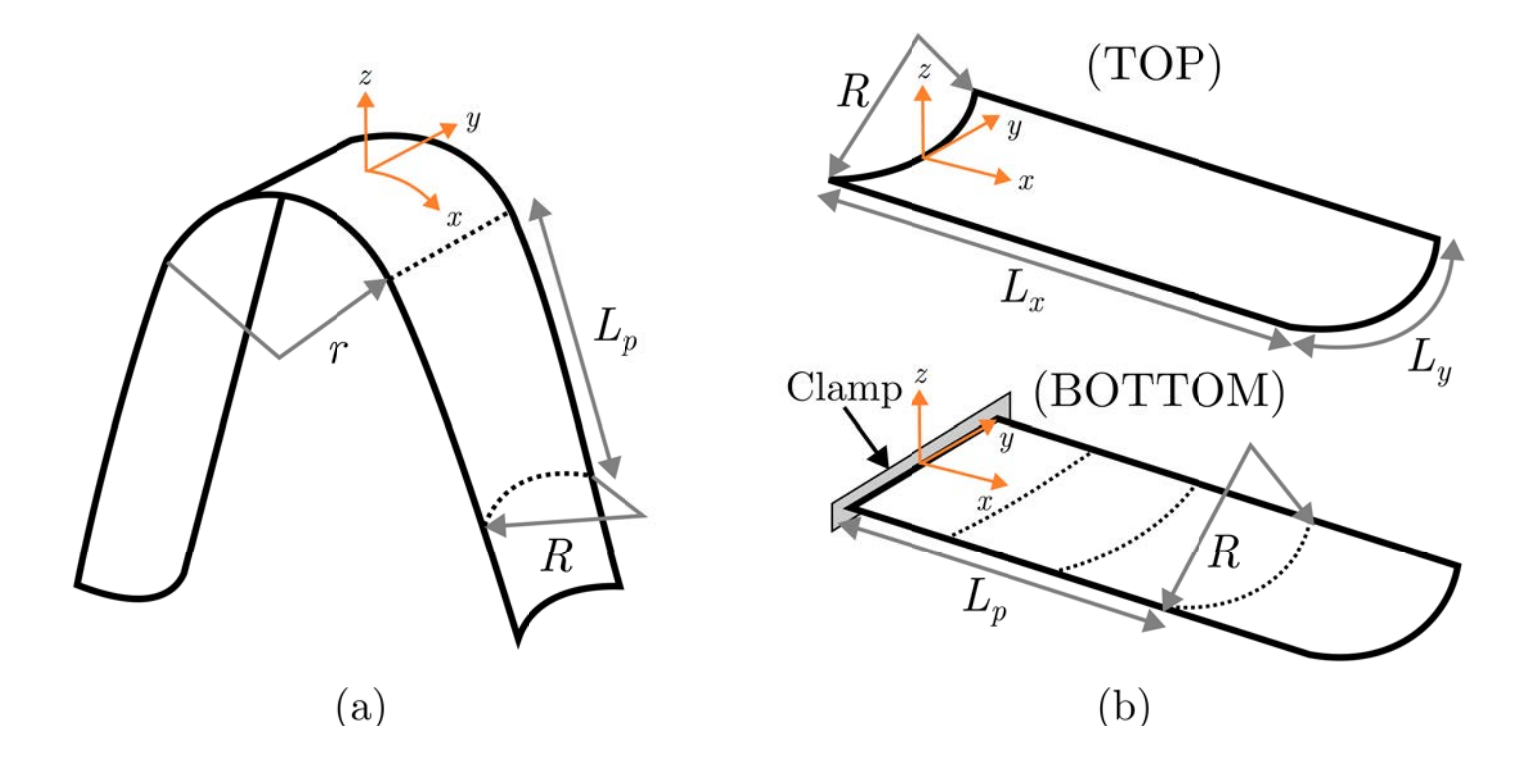


Figure 3: (a) Schematic of a folded tape spring highlighting the central fold and the ploy length, L_p . (b) Schematics of the laminate in state 1 without the clamp BC (TOP) showing a uniform transverse curvature and a zero longitudinal curvature, and the laminate after its edge being clamped (BOTTOM) illustrating the curvature recovery over the ploy length (L_p) .

moments while calculating the strain energy. We limit our analysis to laminates with a cross-ply layup (only 0° or 90° plies) to ensure a uniform initial transverse curvature in state 1. The material properties of a generic transversely isotropic material are given by:

$$E_{11} = E, \quad E_{22} = \beta E, \quad G_{12} = \eta E, \quad \nu_{21} = \nu, \quad \nu_{12} = \nu_{21} \frac{E_{11}}{E_{22}} = \frac{\nu}{\beta},$$
 (2)

where β is the modular ratio. Note that for an isotropic material, $\beta = 1$ and $\eta = 1/2(1+\nu)$. A plane-stress assumption simplifies the constitutive relations between the in-plane stresses (σ) and mid-plane strains (ε) in the laminate, yielding:

$$\boldsymbol{\sigma} = \begin{cases} \sigma_{xx} \\ \sigma_{yy} \\ \sigma_{xy} \end{cases} = \begin{bmatrix} Q_{11} & Q_{12} & 0 \\ Q_{12} & Q_{22} & 0 \\ 0 & 0 & Q_{66} \end{bmatrix} \begin{cases} \varepsilon_{xx} \\ \varepsilon_{yy} \\ 2\varepsilon_{xy} \end{cases} = \mathbb{Q}\boldsymbol{\varepsilon}, \tag{3}$$

where \mathbb{Q} is the reduced stiffness matrix for a 0° oriented ply with:

$$Q_{11} = \frac{E}{1 - \nu^2/\beta}, \quad Q_{12} = \frac{E\nu}{1 - \nu^2/\beta}, \quad Q_{22} = \frac{E\beta}{1 - \nu^2/\beta}, \quad \text{and} \quad Q_{66} = \eta E.$$
 (4)

For a 90° ply, the reduced stiffness matrix can be obtained by simply interchanging the Q_{11} and Q_{22} terms in the above matrix. The extension (\mathbb{A}), extension-bending coupling (\mathbb{B}), and bending (\mathbb{D}) stiffness matrices are then calculated based on the Classical Lamination Theory (CLT) [63] as follows:

$$A_{ij} = \sum_{m=1}^{n_{ply}} \{Q_{ij}\}_m (z_m - z_{m-1}), \qquad (5a)$$

$$B_{ij} = \frac{1}{2} \sum_{m=1}^{n_{ply}} \{Q_{ij}\}_m \left(z_m^2 - z_{m-1}^2\right), \tag{5b}$$

$$D_{ij} = \frac{1}{3} \sum_{m=1}^{n_{ply}} \{Q_{ij}\}_m \left(z_m^3 - z_{m-1}^3\right), \tag{5c}$$

where i, j = 1, 2, 6 as in the reduced stiffness matrix, n_{ply} is the number of plies in the layup, and z is the distance of the ply from the mid-plane. For cross-ply laminates, $A_{16} = A_{26} = B_{16} = B_{26} = D_{16} = D_{26} = 0$.

3.2. Curvature changes and strains

The clamped boundary condition causes a change in the mid-surface curvatures from their initial values. This change of curvatures are represented by $\chi = \{\chi_{xx}, \chi_{yy}, \chi_{xy}\}^T = \kappa - \kappa^0$, where κ^0 is the vector of initial curvatures given by:

$$\kappa^{0} = \begin{Bmatrix} \kappa_{xx}^{0} \\ \kappa_{yy}^{0} \\ \kappa_{xy}^{0} \end{Bmatrix} = \begin{Bmatrix} 0 \\ 1/R \\ 0 \end{Bmatrix}. \tag{6}$$

The strains due to curvature changes vary linearly with the distance from mid-plane, z, through the shell thickness according to Kirchhoff's hypothesis [64]: $\varepsilon = z\chi$. Seffen et al. [38] use an extensible shell model based on Donnell equations to derive expressions for the in-plane and twisting curvature changes. Considering their work, we assume that the double rate of change of longitudinal curvature change along the laminate's length, $\partial^2 \chi_{xx}/\partial x^2$, is small but not negligible compared to that of the transverse curvature change, $\partial^2 \chi_{yy}/\partial x^2$, and that the axial strain, ε_{xx} , dominates over ε_{yy} and ε_{xy} . Hence, we get the following expression:

$$\varepsilon_{yy} \approx 0,$$
 (7a)

$$\varepsilon_{xy} \approx 0.$$
 (7b)

The expressions for the changes in curvatures are given by:

$$\chi_{xx} = -\frac{k^2}{R} \cdot \exp\left(\frac{-k\pi x}{L_y}\right) \left[1 - \cos\left(\frac{\pi y}{L_y}\right)\right],\tag{8a}$$

$$\chi_{yy} = -\frac{1}{R} \cdot \exp\left(\frac{-k\pi x}{L_y}\right) \cos\left(\frac{\pi y}{L_y}\right),\tag{8b}$$

$$\chi_{xy} = \frac{k}{R} \cdot \exp\left(\frac{-k\pi x}{L_y}\right) \sin\left(\frac{\pi y}{L_y}\right),$$
(8c)

where k is a decay parameter with a value typically lower than 1. The Gauss compatibility condition holds true for the laminate:

$$\frac{\partial^2 \varepsilon_{xx}}{\partial y^2} - 2 \frac{\partial^2 \varepsilon_{xy}}{\partial x \partial y} + \frac{\partial^2 \varepsilon_{yy}}{\partial x^2} = \kappa_{xy}^2 - \kappa_{xx} \kappa_{yy}. \tag{9}$$

Expressing the current curvatures in the form of curvature changes and initial curvatures as $\kappa = \chi + \kappa^0$ and equating ε_{yy} and ε_{xy} to zero (see Eq. (7)) in Eq. (9), we get:

$$\frac{\partial^2 \varepsilon_{xx}}{\partial y^2} = -\chi_{xx}\chi_{yy} - \frac{\chi_{xx}}{R} + \chi_{xy}^2. \tag{10}$$

The axial strain can then be computed by integrating the above expression twice with respect to y and finding the constants of integration from $\int_{-L_y/2}^{L_y/2} \varepsilon_{xx} dy = 0$ as:

$$\varepsilon_{xx} = \frac{k^2}{R^2} \cdot \left[\exp\left(\frac{-k\pi x}{L_y}\right) + \exp\left(\frac{-2k\pi x}{L_y}\right) \right] \cdot \left[\frac{y^2}{2} + \frac{L_y^2}{\pi} \cos\left(\frac{\pi y}{L_y}\right) - \frac{L_y^2}{24} - \frac{2L_y^2}{\pi^3} \right]. \tag{11}$$

3.3. Strain energy

3.3.1. Stretching strain energy

The stretching energy is dependent on the extensional stiffness matrix and in-plane strains. The stretching strain energy density per unit surface area of the laminate is calculated as:

$$U_S = \frac{1}{2} \boldsymbol{\varepsilon}^T \mathbb{A} \boldsymbol{\varepsilon} = \frac{1}{2} A_{11} \varepsilon_{xx}^2. \tag{12}$$

3.3.2. Bending strain energy

The bending energy is a function of the bending stiffness matrix and mid-surface curvature changes. The bending strain energy density of the laminate is calculated as:

$$U_B = \frac{1}{2} \boldsymbol{\chi}^T \mathbb{D} \boldsymbol{\chi} + U_B^{ps} = \frac{1}{2} \left(D_{11} \chi_{xx}^2 + 2D_{12} \chi_{xx} \chi_{yy} + D_{22} \chi_{yy}^2 + D_{66} \chi_{xy}^2 \right) + \left(\frac{1}{2} M_{xx}^{ps} \chi_{xx} + \frac{1}{2} M_{yy}^{ps} \chi_{yy} \right). \tag{13}$$

In the above equation, the bending energy due to prestress, $U_B^{ps} = 1/2 \ M_{xx}^{ps} \chi_{xx} + 1/2 \ M_{yy}^{ps} \chi_{yy}$, is included in addition to the bending energy caused by changes in the curvature of the laminate [65]. Here, M_{xx}^{ps} and M_{yy}^{ps} are the residual x and y direction internal bending moments, respectively, which are stored in the laminate after curing. From Eq. (8), it can be seen that $\chi_{xx}^2 \sim k^4/R^2$, $\chi_{yy}^2 \sim 1/R^2$, $\chi_{xx}\chi_{yy} \sim k^2/R^2$, and $\chi_{xy}^2 \sim k^2/R^2$. Therefore, the χ_{yy}^2 term dominates the bending energy as k < 1. Equation (13) can then be reformulated as:

$$U_B = \frac{1}{2}D_{22}\chi_{yy}^2 + \frac{1}{2}M_{xx}^{ps}\chi_{xx} + \frac{1}{2}M_{yy}^{ps}\chi_{yy}.$$
 (14)

3.3.3. Coupled stretching-bending strain energy

The coupled stretching-bending energy exists because of a non-zero coupling matrix, \mathbb{B} , in the case of unsymmetric laminates. This coupled energy is a function of the coupling stiffness matrix, the in-plane strains, and the curvature changes. The coupled stretching-bending strain energy density of the laminate is calculated as:

$$U_C = \frac{1}{2} \boldsymbol{\varepsilon}^T \mathbb{B} \boldsymbol{\chi} + \frac{1}{2} \boldsymbol{\chi}^T \mathbb{B} \boldsymbol{\varepsilon} = B_{11} \varepsilon_{xx} \chi_{xx} + B_{12} \varepsilon_{xx} \chi_{yy}. \tag{15}$$

3.3.4. Total strain energy

The total strain energy of the laminate is found by adding the individual contributions from stretching, bending, and coupling energy densities and integrating them over the surface of the laminate. As the curvature changes and strains decay along the length, we can consider an infinitely long laminate and find the length of the ploy region over which the initial curvature is recovered:

$$\bar{U} = \bar{U}_S + \bar{U}_B + \bar{U}_C = \int_{-L_y/2}^{L_y/2} \int_0^\infty U_S \, dx dy + \int_{-L_y/2}^{L_y/2} \int_0^\infty U_B \, dx dy + \int_{-L_y/2}^{L_y/2} \int_0^\infty U_C \, dx dy. \tag{16}$$

The optimum decay parameter, k, is calculated by minimizing the total strain energy, \bar{U} , of the laminate with respect to k as:

$$\frac{\partial \bar{U}}{\partial k} = \frac{\partial \bar{U}_S}{\partial k} + \frac{\partial \bar{U}_B}{\partial k} + \frac{\partial \bar{U}_C}{\partial k} = 0. \tag{17}$$

The ploy length is then defined as the exponential index in the expression for χ_{yy} :

$$L_p = \frac{L_y}{\pi k}. (18)$$

The exponential index in Eq. (8) at $x = L_p$ is equal to -1, which indicates only a 63% reduction in the curvature change at the clamped edge. Therefore, it is more useful to investigate the decaying variation of χ_{yy} across the length of the laminates to develop a criterion that decides the loss of bistability.

4. Criterion for loss of bistability

The model described in Sec. 3 is employed to calculate the decaying variation of the curvature changes shown in Eq. (8) by first computing the decay parameter from Eq. (17). The total strain energy depends on the \mathbb{A} , \mathbb{B} , and \mathbb{D} matrices. In the following, we establish the value of χ_{yy} for two different cases: prestressed isotropic laminates and prestressed orthotropic laminates.

4.1. Prestressed isotropic laminates

The extensible shell model has been shown to agree with FEA results for several isotropic tape springs in Ref. [38]. We now extend their model to prestressed isotropic bistable laminates. These laminates are manufactured by creating residual stresses by bending the isotropic laminate beyond its yield point [65]. Bistability is induced after the laminate is bent plastically in two different bending directions, generating prestresses σ_{xx} and σ_{yy} . To calculate the prestress, we begin our analysis with a flat plate and follow the manufacturing process already studied in Ref. [65]. The plate is first bent to induce y direction curvature until it permanently deforms and then released for elastic recovery (spring back). In a subsequent step, the sheet is bent in the x direction and released for a final springback. The final prestress values are utilized as inputs for our FE and analytical models. Numerical parameters presented in Sec. 2 are utilized for the isotropic laminates' simulation. Prestress is calculated along the laminate thickness following Ref. [65] and applied as a thermal prestress following the procedure described in Appendix A. The laminates are assumed to be made of a Beryllium Copper (Be-Cu) alloy with material properties E = 130 GPa, $\nu = 0.3$, $\beta = 1$, and $G = E/2(1 + \nu)$. For an isotropic material, the terms in the stiffness matrices that appear in the strain energy formulation (Eq. (16)) are:

$$A_{11} = \frac{Et}{(1 - \nu^2)}, \quad B_{11} = B_{12} = 0, \quad D_{22} = D,$$
 (19)

where $D = Et^3/12(1 - \nu^2)$ is the flexural rigidity. The integrals in Eq. (16) are then evaluated using the symbolic manipulation software *Mathematica* yielding:

$$\bar{U}_S = S \cdot \frac{EtL_y^6 k^3}{R^4 (1 - \nu^2)},\tag{20a}$$

$$\bar{U}_B = B \cdot \frac{DL_y^2}{R^2k} + B_{xx}^{ps} \cdot \frac{L_y^2 k M_{xx}^{ps}}{R} + B_{yy}^{ps} \cdot \frac{L_y^2 M_{yy}^{ps}}{Rk}, \tag{20b}$$

$$\bar{U}_C = 0, (20c)$$

where the numerical pre-factors have the values $S \simeq 9.17 \times 10^{-6}$, $B \simeq 0.039$, $B_{xx}^{ps} \simeq -0.058$, and $B_{yy}^{ps} \simeq -0.101$. Note that $\bar{U}_C = 0$ for an isotropic material because the coupling matrix vanishes, $\mathbb{B} = [0]$. Substituting Eq. (20) in Eq. (17) gives a fourth-order equation in k as shown below:

$$\left(36S \cdot EtL_{y}^{4}\right)k^{4} + \left(12B_{xx}^{ps} \cdot M_{xx}^{ps}R^{3}\left(1 - \nu^{2}\right)\right)k^{2} + \left(12B_{yy}^{ps} \cdot M_{yy}^{ps}R^{3}\left(1 - \nu^{2}\right)\right)k - \left(B \cdot Et^{3}R^{2}\right) = 0.$$
 (21)

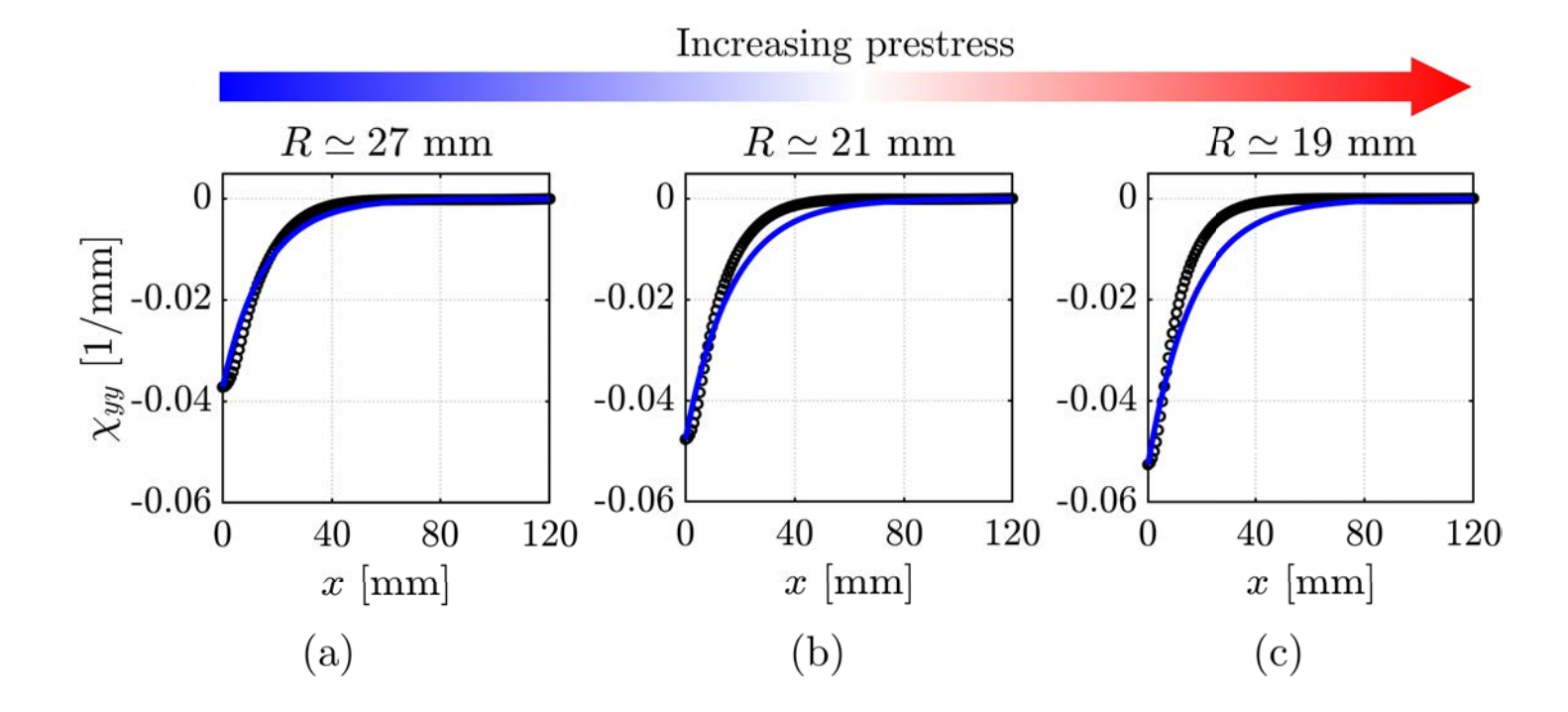


Figure 4: Change in transverse curvature, χ_{yy} , vs the distance from the clamped edge from FEA (black circular markers) and the extensible model (blue solid line) for an isotopic prestressed laminate with $L_x = 150$ mm, $L_y = 20$ mm, and t = 0.1 mm for three different initial radii of curvature: (a) $R \approx 27$ mm, (b) $R \approx 21$ mm, and (c) $R \approx 19$ mm.

The values of R, M_{xx}^{ps} , and M_{yy}^{ps} are obtained from FEA, but they can also be found analytically using a Rayleigh-Ritz energy minimization approach (see Appendix B). The transverse curvature changes predicted by the model are compared with FEA simulations with generally good agreement for a 150 mm \times 20 mm laminate with three different values of prestress (and initial radius) in Fig. 4. The results are only plotted until x = 120 mm to avoid the free boundary effects close to the x = 150 mm edge in FEA output. As the prestress is increased, the initial curvature of state 1 increases. In Fig. 4, the induced prestress increases from the left to the right. The extensible model shows good agreement for the χ_{yy} decay, showing a slightly slower variation than that observed in FEA, which is regarded as the "true/reference decay." This slight difference can possibly be attributed to the assumption of zero ε_{yy} and ε_{xy} in the model when the edge is clamped. In contrast, in the FE simulations, these strains are small but not negligible because of the initial prestress present in the structure. For each of the cases in Fig. 4, we consider the laminate length at which χ_{yy} is $1\%^1$ of its value at the clamp to represent the "complete recovery" of initial curvature. For R = 27, 21, and 19 mm, the model predicts these lengths to be 71, 78, and 79 mm, respectively. Because the laminates' initial curvature is recovered at a distance from the clamp which is lower than their length, the laminates would be able to retain their state 1 in the presence of a clamped BC. This result is supported by FE simulations which show that the isotropic laminate is bistable for all three prestress values shown in Fig. 4. Our FE results show that the complete curvature need not be recovered at the laminates' free edge for them to be bistable when clamped. Based on preliminary

¹99% curvature recovery is selected given the asymptotic behavior of the exponential term in Eq. 8.

observations, these laminates retain their bistable behavior even when the curvature change at their free edge is 10% of the value at the clamp. Estimating a relation between the prestress and the allowable percentage of curvature recovery at the free edge to retain bistability would require analyzing a wide range of geometries, materials, and prestress conditions using FEA. However, the results from our analytical model reveal that if the laminates are sufficiently long to recover 99% of their initial curvature in state 1 after clamping, then bistability is guaranteed. Although this is a conservative estimate, the obtained metric is advantageous for designing isotropic laminates that retain their bistability even after clamping.

4.2. Prestressed orthotropic laminates

We now consider a generic composite laminate with a width, L_y , equal to 100 mm, and the material properties listed in Table 1. The model parameters as in Eq. (2) for this material are E = 140 GPa, $\beta \simeq 0.067$, $\nu \simeq 0.02$, and $\eta \simeq 0.036$. We choose a cross-ply unsymmetric layup of $[90/0]_T$ for simplicity. For this layup, the terms in the stiffness matrices that appear in the strain energy formulation can be calculated as:

$$A_{11} = \frac{Et}{(1 - \nu^2/\beta)} \cdot \frac{(1 + \beta)}{2}, \quad B_{11} = \frac{Et^2}{8(1 - \nu^2/\beta)} \cdot (1 - \beta), \quad B_{12} = 0, \quad D_{22} = D \cdot \frac{(1 + \beta)}{2}. \tag{22}$$

The flexural rigidity for an orthotropic material is given by $D = Et^3/12 (1 - \nu^2/\beta)$. The strain energies are then computed as follows:

$$\bar{U}_S = S \cdot \frac{EtL_y^6 k^3 (1+\beta)}{R^4 (1-\nu^2/\beta)},$$
(23a)

$$\bar{U}_B = B \cdot \frac{DL_y^2 (1+\beta)}{R^2 k} + B_{xx}^{ps} \cdot \frac{L_y^2 k M_{xx}^{ps}}{R} + B_{yy}^{ps} \cdot \frac{L_y^2 M_{yy}^{ps}}{R k}, \tag{23b}$$

$$\bar{U}_C = C \cdot \frac{Et^2 L_y^4 k^3 (\beta - 1)}{R^3 (1 - \nu^2 / \beta)},$$
(23c)

where $S \simeq 4.59 \times 10^{-6}$, $B \simeq 0.019$, $B_{xx}^{ps} \simeq -0.058$, $B_{yy}^{ps} \simeq -0.101$, and $C \simeq 6.15 \times 10^{-5}$. As for the isotropic case, R, M_{xx}^{ps} , and M_{yy}^{ps} are obtained using FEA, but the Rayleigh-Ritz approach can also be used instead (see Appendix B). Again, a fourth-order equation is obtained, which can be solved for the decay parameter value for the chosen orthotropic material and prestress moments. Figure 5 shows the variation of χ_{yy} with the distance from the clamp obtained from the extensible model and FEA for a 350 mm \times 100 mm orthotropic laminates with three different levels of prestress ($\Delta T = -70^{\circ} \text{C}$, -110°C , and -150°C). It must be noted that state 1 is not stable for this geometry. The curvature change from FEA shown in Fig. 5 corresponds to the (out-of-equilibrium) instant when the edge has just been clamped, and the laminate is about to start switching to state 2. Results are plotted only until x = 300 mm to avoid edge effects. As the prestress increases, state 1's radius of curvature decreases (left to right in Fig. 5). Similar to the isotropic case, the model predicts a decaying χ_{yy} along x, but the predicted decay variation is lower than that observed from FE results. The difference from FEA is higher in this case than the isotropic one, possibly because the laminate's width relative to its length (L_y/L_x) has a greater value, implying

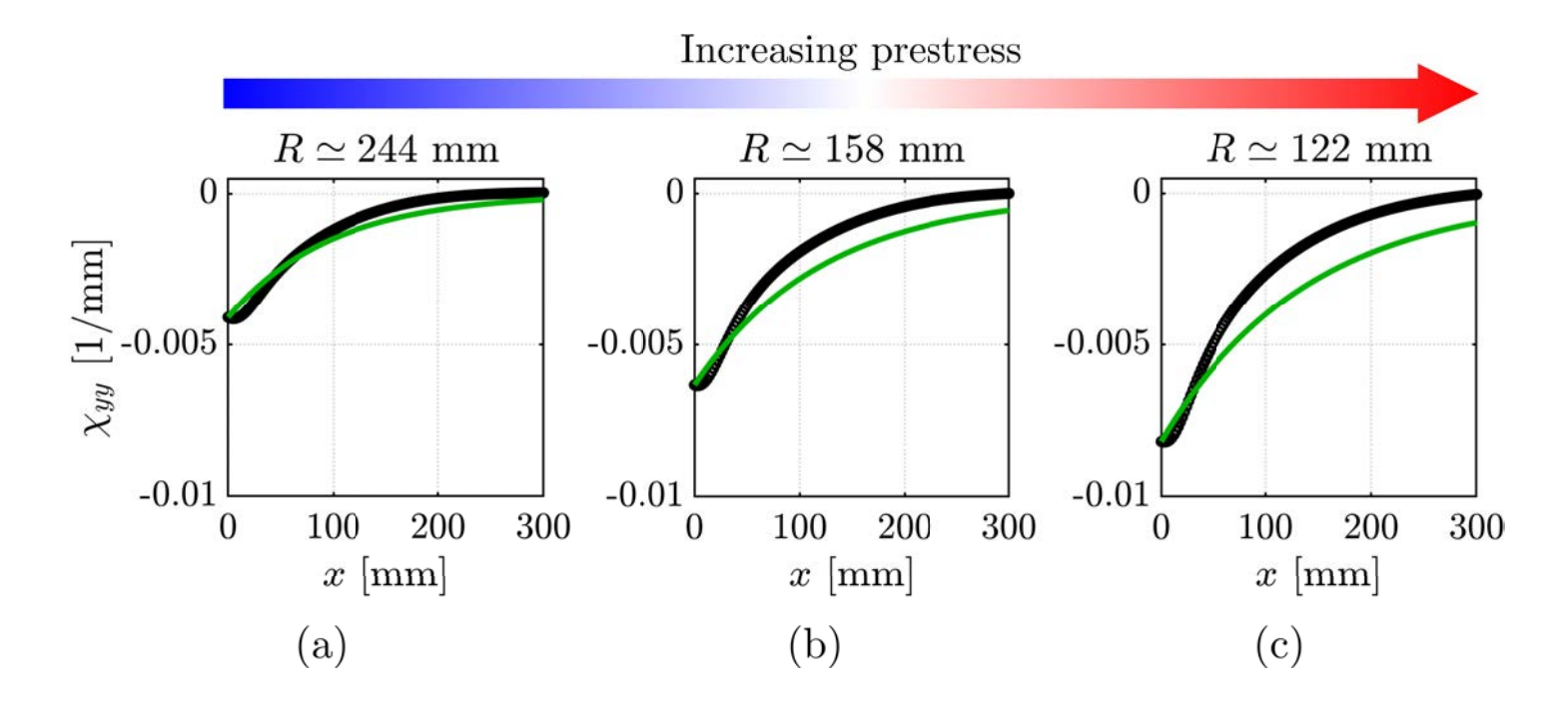


Figure 5: Change in transverse curvature, χ_{yy} , vs the distance from the clamped edge from FEA (black circular markers) and the extensible model (green solid line) for an orthotropic prestressed laminate with $L_x = 350$ mm, $L_y = 100$ mm, and t = 0.24 mm for three different initial radii of curvature: (a) $R \approx 244$ mm, (b) $R \approx 158$ mm, and (c) $R \approx 122$ mm.

that the rate of axial change in longitudinal curvature ($\partial^2 \chi_{xx}/\partial x^2$) has a larger value [52]. Considering a 99% recovery of initial curvature, the distances from the clamp at which this is observed are 454 mm for $R \simeq 244$ mm, 568 mm for $R \simeq 158$ mm, and 644 mm for $R \simeq 122$ mm. These distances are much larger than those observed in isotropic materials in Sec. 4.1, because the stress (and curvature change) decay is less pronounced in orthotropic materials when compared to isotropic cases [54]. The generic laminate chosen here is not bistable for any of the prestress values shown in Fig. 5 because the corresponding 99% decay lengths are larger than the laminate's length (350 mm). Even with the steeper decay observed in FEA, the laminate length is not sufficient for the transverse curvature changes to reach 1% of their value at the clamp, thereby causing a loss of bistability.

A relatively steeper curvature change decay along the laminate's length is observed in orthotropic materials as the modular ratio, β , is increased [38]. For the same geometry of the $[90/0]_T$ laminate as before and a thermal prestress of $\Delta T = -110^{\circ}\mathrm{C}$, the modular ratio is varied between 0.01 to 1 to observe the length from the clamp where there a 99% decay of the transverse curvature change, χ_{yy} . Figure 6 shows the effect of β on the 99% decay length from the laminate's clamped edge predicted by the extensible model. It is observed that the decay is much steeper for higher values of β , which results in a lower length required to reach 1% initial curvature of state 1 threshold for retaining bistability. The transverse bending moment resultant contours (SM2) in the clamped laminate just before it switches to state 2 are also shown in Fig. 6 for three different modular ratios, indicating a clear increase in the decay rate for larger β values. Even at $\beta = 1$, the minimum length required to retain state 1 after clamping is greater than 400 mm, similar to that observed using FEA. Consequently, guaranteeing bistability for unsymmetric laminates according to this criterion requires aspect ratios much larger than 1, which is unrealistic for practical applications.

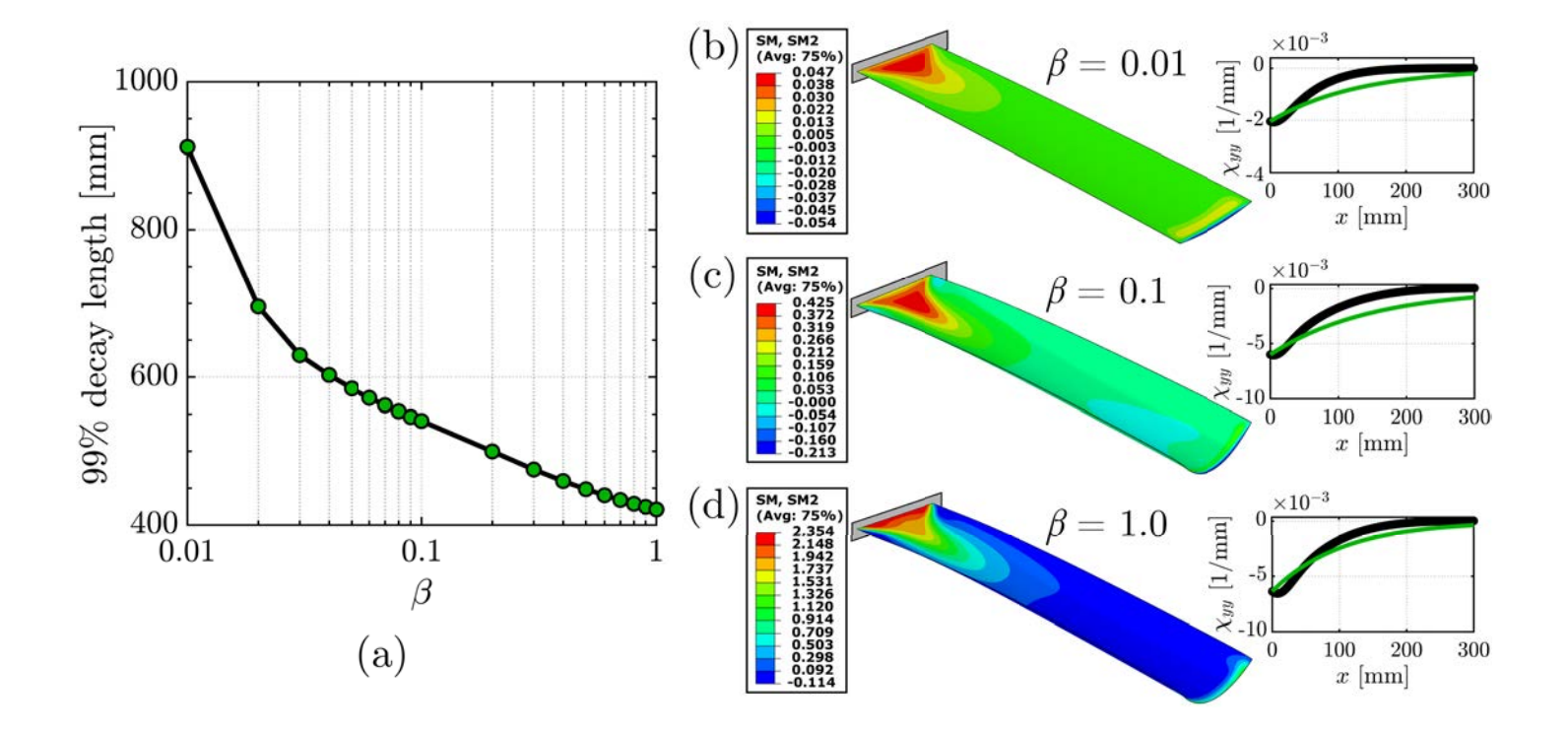


Figure 6: (a) 99% decay length predicted by the extensible model vs the modular ratio, β , of a 350 mm × 100 mm laminate with a $[90/0]_T$ layup. The 99% decay length decreases as β is increased, indicating a lower minimum length required to retain state 1 after clamping as β increases. The transverse bending moment resultant contours after clamping the x = 0 mm edge for (b) $\beta = 0.01$, (c) $\beta = 0.1$, and (d) $\beta = 1.0$ are shown on the right illustrating a steeper decay at higher modular ratios. The plots in the insets next to the respective contours show the comparison of χ_{yy} along the laminate's centerline between the extensible model (green solid line) and FEA (black circular markers) showing a good agreement for all three modular ratios.

Therefore, alternative methods to retain bistability in orthotropic prestressed laminates without the need to increase their aspect ratios are necessary, as discussed in the following section.

5. Symmetric transition region to retain bistability

The stacking sequence of a composite dictates its post-cure shape and structural properties. Consequently, having an additional symmetric $[0_2]_T$ section of length L_s in the laminate's planform starting at the clamp causes a change in the prestress developed while cooling. In contrast to the unsymmetric $[90/0]_T$ section, no stresses are developed in the symmetric layup region due to the temperature change. Hereafter, we refer to this symmetric section as a "prestress-free" or "transition" zone. The transition ratio (TR) is then defined as shown below:

$$TR = \frac{L_s}{L_x}. (24)$$

AR and TR collectively define the geometry of a two-section laminate. As stated in Sec. 3, the curvature in either state appears only because of the thermal prestress induced in the laminate. As

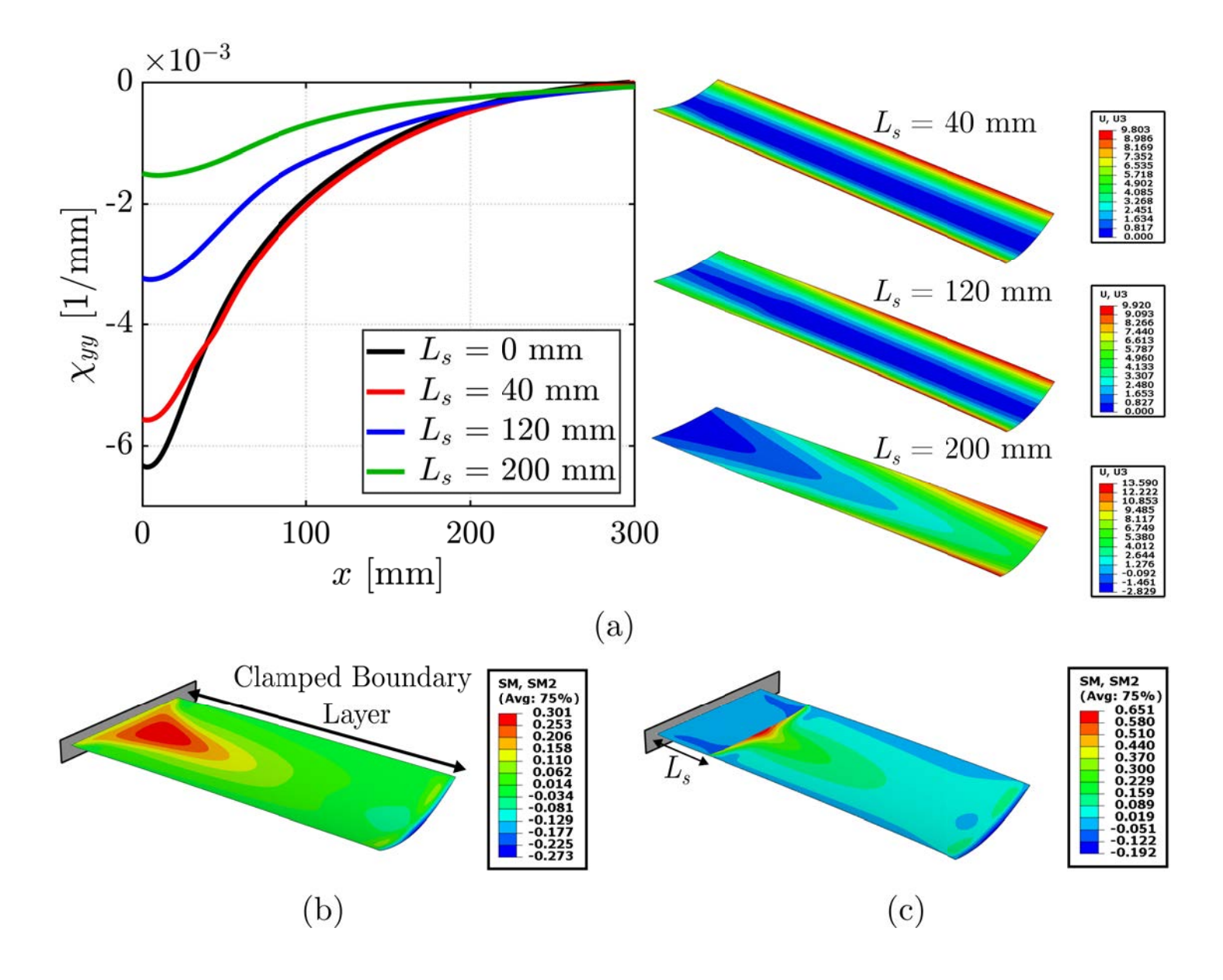


Figure 7: (a) Curvature changes vs length along the longitudinal centerline of a 350 mm \times 100 mm laminate with varying transition zone sizes obtained from finite element simulations. The displacement contours for free-free laminates with $L_s=40$ mm, 120 mm, and 200 mm from FEA are shown on the right with decreasing edge transverse curvature as L_s increases. The deflections shown in the contours are in mm. (b) Transverse bending moment resultant contour showing the boundary layer produced by clamping one edge of a bistable laminate with AR=2. Without the prestress-free zone, the boundary layer produced by clamping interacts with the free edge boundary layer just before the laminate loses its bistability. (c) Introducing a prestress-free transition zone with TR=0.2 preserves bistability by abruptly discontinuing the clamped boundary layer at the interface between sections.

the prestress is reduced, the curvature of both states also decreases. Because the symmetric section experiences no prestress, it does not exhibit any out-of-plane warping by itself. However, when connected to the unsymmetric section of the laminate, out-of-plane warping is induced as a result of internal residual

loads in the laminate. It is observed that as TR increases, the symmetric region spans a larger area and consequently, the curvature of x=0 edge decreases. The transverse curvature change, χ_{yy} , along the longitudinal centerline, y=0, of a laminate with $L_y=100$ mm and AR=3.5 is plotted for different L_s values in Fig. 7a. It can be seen that χ_{yy} decays along the length of the laminate even with the presence of a prestress-free zone similar to the fully prestressed laminate ($L_s=0$). Because of an increase in L_s , the prestress in the structure decreases, which in turn reduces the initial curvature before clamping. Clamping the laminate induces a transverse bending moment close to the edge, producing a boundary layer that decays along the length of the laminate. Figure 7b shows the clamped boundary layer produced in state 1 when no transition zone is present, just before the laminate switches to state 2. This clamped boundary layer interacts with the boundary layer produced at the free edge. In the presence of a stress-free zone, however, there is an abrupt disruption of the clamped boundary layer at the interface between the symmetric and unsymmetric sections of the laminate, as can be seen in Fig. 7c. Therefore, the geometry of the transition region impacts the clamped edge boundary layer, affecting the laminate's resulting stable shapes. This disruption of the clamped boundary layer preserves state 1 of the laminate despite the clamped BC. The following analysis sheds light on the origin of this effect.

5.1. Extensible shell model for multi-section composite laminates

A criterion to predict the minimum length of a rectangular cross-ply composite laminate that preserves both its stable states after clamping one of its edges is proposed in Sec. 4. According to this criterion, the minimum length needed for preserving state 1 after clamping is defined as the distance from the clamped edge at which there is a 99% decay of the transverse curvature change, χ_{yy} . The extensible model proposed in Sec. 3 captures the behavior of single-section laminates with a uniform cross-ply layup. In the presence of an additional symmetric layup region close to the clamp, the laminate has two different sections with different layups. Therefore, a single decay parameter can no longer be used to represent the curvature changes along the entire laminate. Furthermore, state 1 of a laminate with two sections does not exhibit a constant initial transverse radius of curvature along its length. Figure 8a shows the initial curvature of a two-section laminate with $L_x = 350$ mm, $L_y = 100$ mm, and t = 0.24 mm for three different symmetric region lengths: $L_s = 40$ mm, 120 mm, and 200 mm obtained using FEA (black solid lines). Although the initial curvature is non-uniform along the length of the laminate, it can be approximated as three different regions with distinctive trends. These regions are the symmetric region with $R1: x \in [0, L_s)$, the interface region with $R2: x \in [L_s, L_i)$, and the developed region with $R3: x \in [L_i, L_x]$, where $0 < L_s < L_i$ is dictated by the distance from $x = L_s$ where κ_{yy}^0 reaches a value within 1% of the fully developed curvature. The symmetric region has a $[0_2]_T$ layup while the interface and developed regions have a $[90/0]_T$ layup. We observed in Fig. 8a that the initial curvature variation follows a linear trend in the symmetric and interface regions, and settles to an almost constant value in the developed region for all three cases. From FEA, the initial transverse curvatures at the region boundaries can be obtained as $\kappa_{yy}^0(x=0)=1/R_0$, $\kappa_{yy}^0 (x = L_s) = 1/R_s$, and $\kappa_{yy}^0 (x \ge L_i) = 1/R$. The initial curvature of state 1 of the laminate can then be approximated as:

$$\kappa_{yy}^{0}(x) = \begin{cases}
\frac{1}{R_0} + \frac{x}{L_s} \left(\frac{1}{R_s} - \frac{1}{R_0} \right), & \text{for } R1 : 0 \le x < L_s \\
\frac{1}{R_s} + \frac{x}{L_i - L_s} \left(\frac{1}{R} - \frac{1}{R_s} \right), & \text{for } R2 : 0 \le x < L_i - L_s \\
\frac{1}{R}, & \text{for } R3 : 0 \le x \le L_x - (L_s + L_i)
\end{cases}$$
(25)

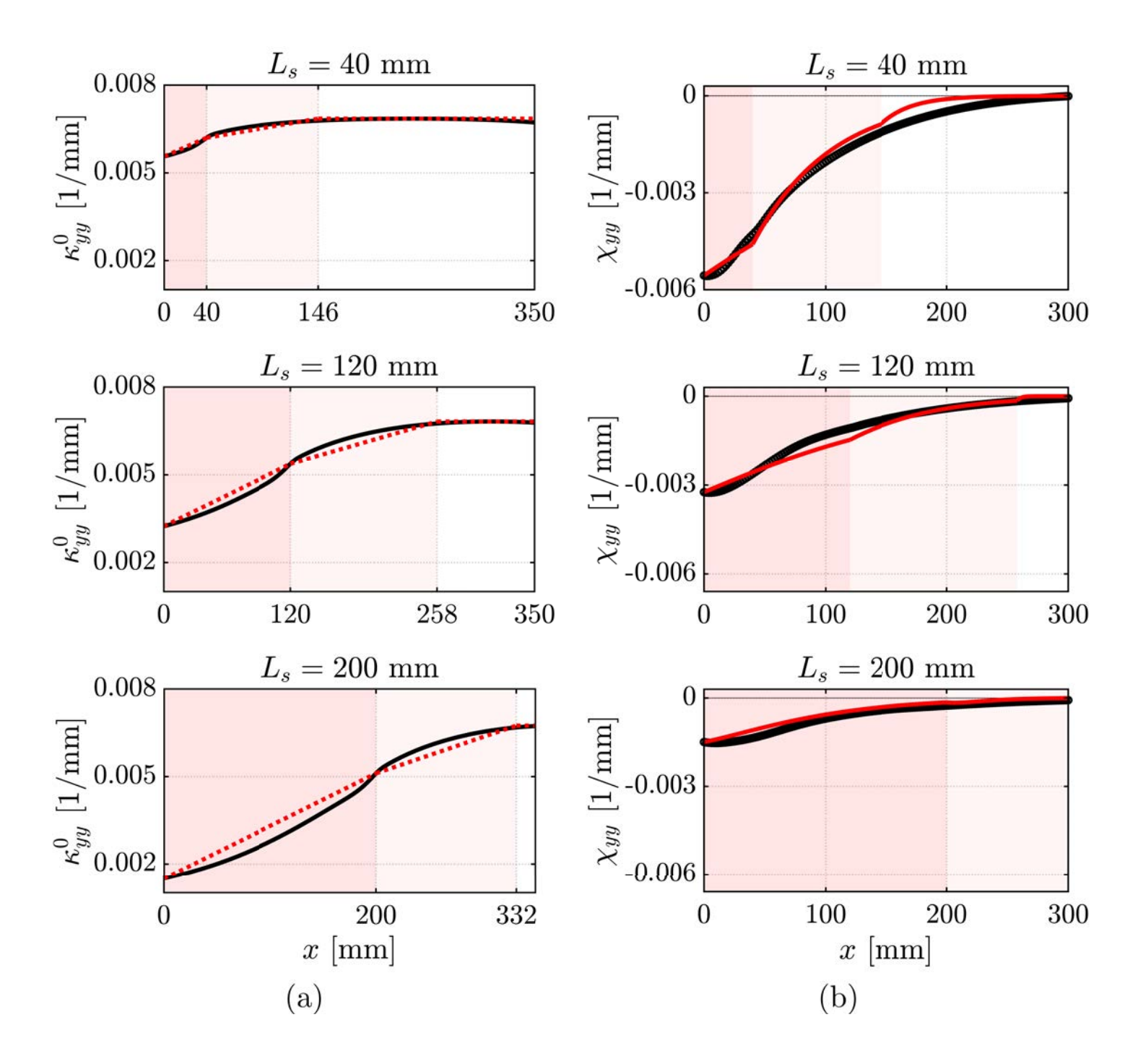


Figure 8: (a) Variation of initial transverse curvature, κ_{yy}^0 , along a 350 mm \times 100 mm laminate's centerline for three different symmetric region lengths: $L_s = 40$ mm, 120 mm, and 200 mm, showing the linear trend in the symmetric (dark shaded) and interface (light shaded) regions, and an almost constant value in the developed (unshaded) region. The interface region domains are marked on the x-axis. The black solid lines are the FEA curvatures while the red dashed lines indicate the approximations used in the model. (b) Change in transverse curvature, χ_{yy} , vs the distance from the clamped edge from FEA (black circular markers) and the two-section extensible model (red solid line) for the laminate demonstrating good agreement for all the chosen L_s values.

These approximated curvatures are plotted as red dashed lines in Fig. 8a showing a close match with FEA results. Higher order (>1) approximations for initial curvatures only marginally increase the accuracy while increasing the computational cost, and are therefore not adopted in our analysis to maintain the simplicity of the model. The y direction curvature changes shown in Eq. (8b) are reformulated as:

$$\chi_{yy}^{R1}(x,y) = -\kappa_{yy}^{0,R1}(x) \cdot \exp\left(\frac{-k^{R1}\pi x}{L_y}\right) \cos\left(\frac{\pi y}{L_y}\right),\tag{26a}$$

$$\chi_{yy}^{R2}(x,y) = \chi_{yy}^{s}(x) \cdot \exp\left(\frac{-k^{R2}\pi x}{L_y}\right) \cos\left(\frac{\pi y}{L_y}\right),\tag{26b}$$

$$\chi_{yy}^{R3}(x,y) = \chi_{yy}^{i}(x) \cdot \exp\left(\frac{-k^{R3}\pi x}{L_y}\right) \cos\left(\frac{\pi y}{L_y}\right), \tag{26c}$$

where $\chi_{yy}^s(x) = \chi_{yy}^{R1}(L_s, 0) - (\kappa_{yy}^{0,R2}(x) - \kappa_{yy}^{0,R2}(0))$ and $\chi_{yy}^i(x) = \chi_{yy}^{R2}(L_i - L_s, 0)$, and the superscripts R1, R2, and R3 correspond to the respective regions. Note that the domain of each individual region is transformed to start at x = 0 to represent the transverse curvature changes as decay functions similar to Sec. 3 while we modify the initial value of χ_{yy} at each region's interface to maintain continuity. χ_{xx} , χ_{xy} , and ε_{xx} are subsequently calculated from the χ_{yy} value obtained from Eq. (26) according to the procedure followed in Ref. [38]. The decay parameters for each section are then found using Eq. (17). The change in transverse curvature along the centerline of the laminate is plotted against x for the aforementioned L_s values in Fig. 8b. These plots are only shown until x = 300 mm to avoid the edge effects in FEA.

The two-section extensible model χ_{yy} predictions (red solid lines) match closely with FEA results (black circular markers). By employing the bistability criterion proposed in Sec. 4, the stability of state 1 under clamped BC is then assessed by finding the distance from the clamp where there is a 99% decay in χ_{yy} . The 99% decay lengths found with our analytical model are 214 mm for $L_s = 40$ mm, 268 mm for $L_s = 120$ mm, and 231 mm for $L_s = 200$ mm, all of which are lower than the laminate's length, $L_x = 350$ mm, thus indicating bistable behavior under clamped BC, similar to that observed from our FE results. Note that for $L_s = 40$ mm and 120 mm, the 99% decay length lies in the developed region, while for $L_s = 200$ mm, the same lies in the interface region. Therefore, our results indicate that the 1% curvature decay criterion developed for single-layup laminates retains its predictive capabilities for two-region laminates. This model can be extended for laminates containing more than two sections using a similar methodology.

5.2. Stability map for two-section laminates

We now choose a laminate geometry with $L_y = 100$ mm to demonstrate the robustness of the presented multi-section extensible model for determining the stability of orthotropic laminates over a wide range of aspect ratios and transition ratios (see Eq. (24)). The chosen laminate consists of a symmetric section $(S1: x \in [0, L_s], y \in [-L_y/2, L_y/2])$ with a $[0_2]_T$ layup and an unsymmetric section $(S2: x \in [L_s, L_x], y \in [-L_y/2, L_y/2])$ with a $[90/0]_T$ layup. The material properties are shown in Tab. 1. Figure 9 shows the stability map of orthotropic laminates with AR between 1 and 3. The transition ratio is varied from 0 (no symmetric region, $L_s = 0$) to 1 (no unsymmetric region, $L_s = L_x$). At TR close to 0, laminates are bistable under free-free BC but lose their bistability once clamped according to both FEA (orange square markers) and the model (orange shaded area).

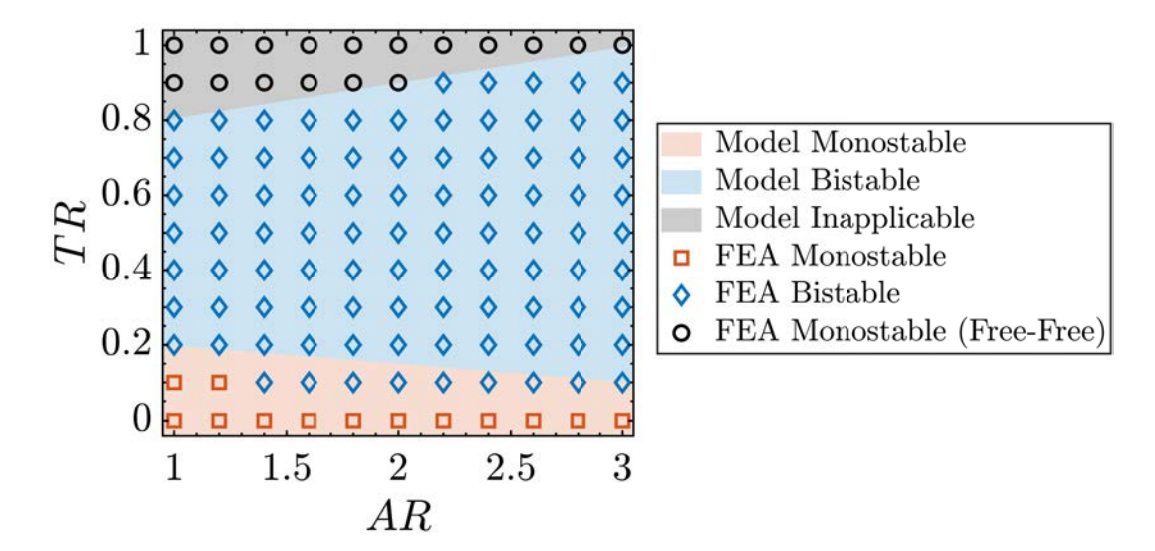


Figure 9: Stability map of rectangular orthotropic laminates by varying the aspect ratio and transition ratio demonstrating the utility of the symmetric transition region in expanding the bistability domain in the presence of a clamped BC. The shaded areas are the results from the multi-section extensible model while the markers indicate outputs from FEA.

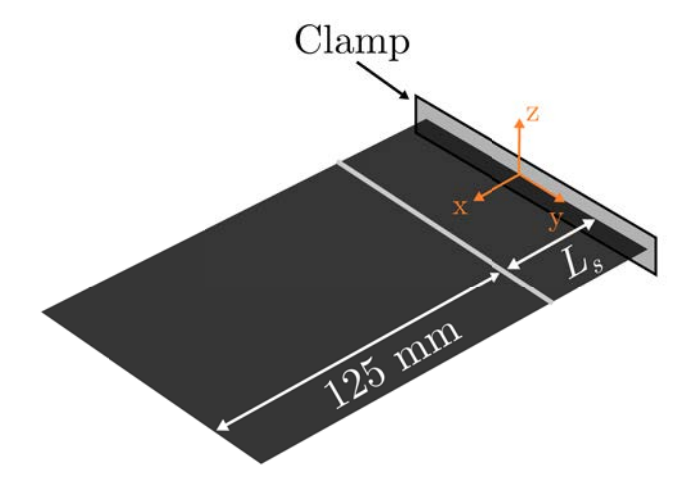


Figure 10: Geometry of the clamped laminate used in experiments with a constant unsymmetric section length of 125 mm and a varying symmetric region length, L_s .

On the other hand, at TR close to 1, the prestress developed in the laminates is negligible which eliminates state 2 under free-free BC. The extensible model is only defined for laminates that exhibit both state 1 and state 2 before clamping and is therefore inapplicable in this regime as indicated by the grey shaded area in Fig. 9. The obtained results using FEA (blue diamond markers) and the derived multisection model (blue shaded area) show that introducing a symmetric transition region with $0.2 \le TR \le 0.8$ yield bistable laminates even after imposing a clamped BC for all aspect ratios. At low TR (0.1), the model slightly overpredicts the transition ratio required to preserve bistability after clamping for AR > 1.2. Our results indicate that the derived model thus gives a conservative estimate for designing bistable laminates with clamped boundary conditions.

6. Experimental validation

We validate our multi-section extensible model by manufacturing and clamping an initially bistable laminate. Specifically, a four-layer composite laminate was manufactured using a Grafil TR50S/Newport 301 unidirectional prepreg with material properties shown in Tab. 1. The laminate was 250 mm long and 100 mm wide, and consisted of a symmetric $[0_4]_T$ section and an unsymmetric $[90_2/0_2]_T$ section. Both the sections spanned an equal portion of 125 mm in the longitudinal direction. The plies were laid up in the specified stacking sequence and cured at a temperature of 130°C. The cured laminate was then allowed to cool to room temperature (20°C) to develop state 1 and state 2 under free-free BCs with similar shapes as in Fig. 2a.

To observe the effect of clamped BC on the laminate's bistability with different symmetric region lengths, the entire symmetric section was initially clamped $(L_s = 0)$ and the amount of symmetric section being clamped was decreased in small steps to mimic an increase in L_s (See supplementary material). The geometry of the laminate in the experiment is schematically shown in Fig. 10. When $L_s = 0$, the laminate only exhibited state 2 after clamping as shown in Fig. 11a. The out-of-plane deflections along the longitudinal centerline (y=0) of the clamped laminate in the experiment are compared to FEA with good agreement in the plot shown to the right in this figure. The extensible model also predicts monostability for the chosen laminate without a symmetric transition region. L_s was then increased in steps of 1 mm in FEA, experiments, and the two-section model to determine the minimum L_s value that preserves state 1 in the presence of the clamped BC. The minimum L_s for bistability is found to be 25 mm using the extensible model, 22 mm using FEA, and 20 mm experimentally, thus revealing good agreement between the three cases and validating the predictive capacity of the analytical model in spite of the small differences. The experimental value is slightly lower than that observed in FEA as the clamped BC imposed perfectly blocks all deflections. However, a perfect clamped boundary condition cannot be realized experimentally causing the laminate to retain state 1 at a lower symmetric region length than FEA. The model overestimates the minimum L_s value needed to retain bistability by a small margin when compared to FEA and experiment. This result is in accordance with the prior results shown in Sec. 5 with the model providing a conservative design estimate for bistability. A comparison between the experimental and finite element shapes of state 1 and state 2 of the two-section laminate with $L_s = 22$ mm is shown in Fig. 11b and Fig. 11c respectively. It can be seen that the experimental deflections along the centerline and the free edge of state 1, and along the centerline of state 2, match closely to the FEA predictions.

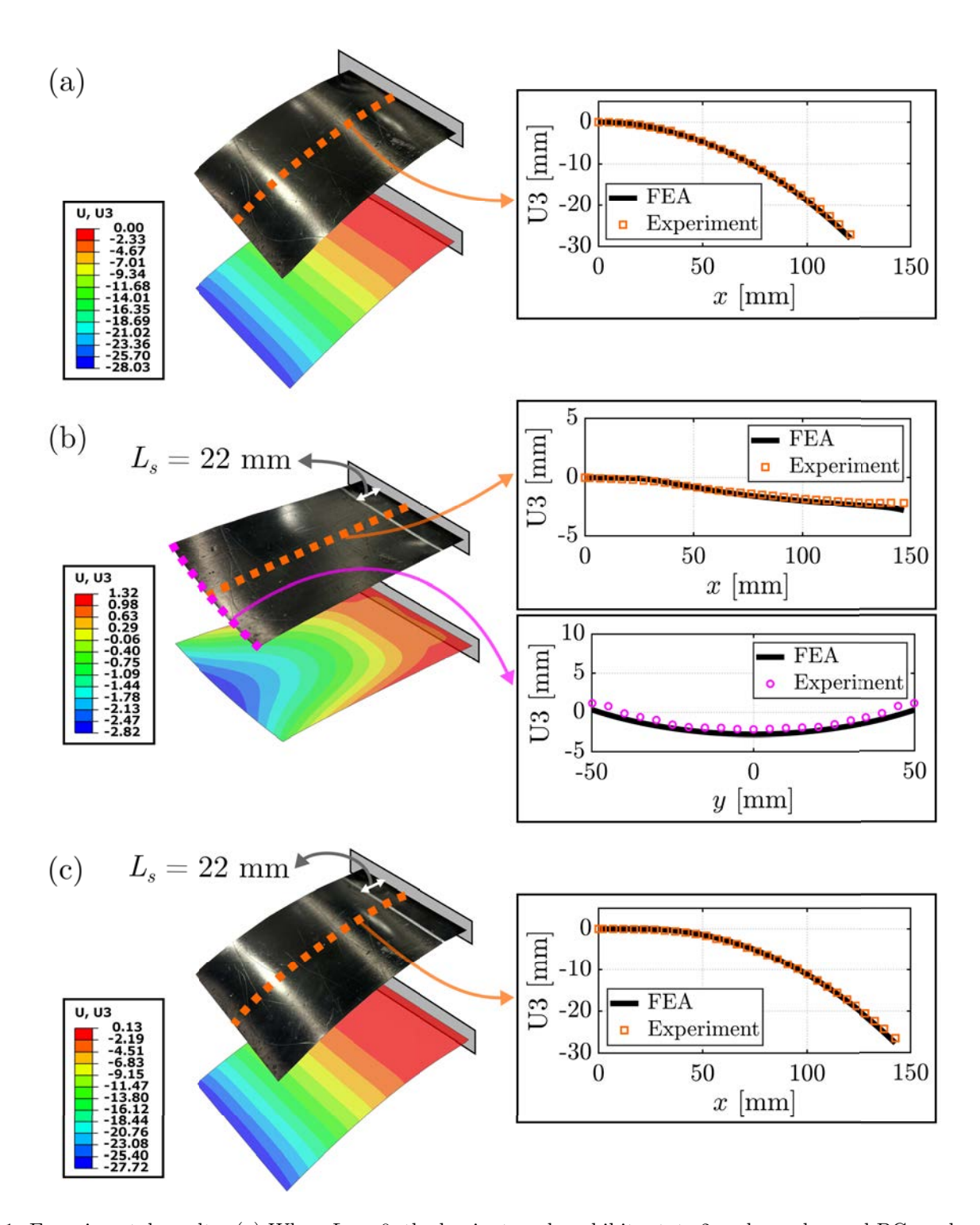


Figure 11: Experimental results: (a) When $L_s = 0$, the laminate only exhibits state 2 under a clamped BC as observed from the experiment (top) and FEA (bottom). The plot on the right is a comparison of the out-of-plane deflections (U3) along the longitudinal centerline of the laminate between FEA and experiment, showing a close match. (b) State 1 and (c) State 2 of the laminate with $L_s = 22$ mm observed in the experiment (top) and using FEA (bottom) illustrating bistability under a clamped BC. The laminate deflections (U3) from FEA and experiment are compared in the plots to the right showing generally good agreement for both stable states. All the deflections in FEA contours shown are in mm.

7. Conclusions

An analytical approach is presented to examine the effect of clamped boundary conditions on prestressed bistable laminates. Clamped boundary decay over the length of the laminate is calculated using an analytical model considering the stretching, bending, and coupling strain energies in the system. An exponential decay is observed in the structure, which is calculated for isotropic and orthotropic materials, showing a strong relation between stress decay, curvature recovery, and loss of bistability. Specifically, we observed that the curvature at the free edge of the laminate needs to fully recover its initial value for the laminate to retain its bistability after clamping an edge. Moreover, a strong correlation between the transverse curvature change decay and material properties is observed, giving unrealistic aspect ratios to retain bistability for the analyzed single-layup composite laminates. To address this strong design constraint, a symmetric transition region was incorporated in previous studies to increase the AR range for which bistability was preserved after clamping. Our analysis reveals the origin behind the effectiveness of introducing such a transition region to act as the discontinuity in stress propagation in such laminates, reducing the effect of the clamped boundary condition. Our analysis further establishes a criterion for retaining bistability after clamping based on the decay to reach within a 1% threshold of original curvature within the laminate's length. Notably, our criterion shows good agreement with FEA and experiments for both single-section and two-section orthotropic laminates. The utility of the prestress-free region in retaining bistability over a wide range of geometries is also demonstrated through FEA. The results presented in this paper affirm the potential of the developed analytical model as a design guideline for cantilevered bistable laminates embedded in larger compliant systems.

As a next step, variations in the transverse strains will be included in the extensible model to improve its curvature prediction for clamped laminates. Future work will also include efforts toward estimating an exact correlation between the prestress and minimum length of the laminate to retain bistability for both the isotropic and orthotropic prestressed laminates to establish a more robust criterion. Furthermore, multi-section laminates with more than one edge clamped will be analyzed to understand the curvature decay in more elaborate systems with multiple boundary conditions, which is relevant for several real-world scenarios.

Data availability

The data that support the findings of this study are available from the corresponding author upon reasonable request.

Acknowledgements

J. C. Osorio and A. F. Arrieta gratefully acknowledge the support from Anheuser-Busch InBev and NSF through the CAREER award No. 1944597.

Appendix A. Thermal analogy for isotropic FE simulations

In this section, we describe the forming process that leads to the bistable behavior of prestressed isotropic laminates. The simplest way to induce residual stress is by deforming it beyond its yield point. The process is started by plastically deforming a flat sheet by applying a bending moment along the edge

(Fig. A.1a). The moment is removed, and the sheet is allowed to relax (Springback), reaching residual curvature κ_x^1 (Fig. A.1b). After this, the sheet is flattened and plastically deformed in the other direction. The two stable states obtained can be observed in Fig. A.1b and Fig. A.1e. For this process, we assumed that the flattening and springback are purely elastic, and no stress passes the ultimate yield stress. It should be mentioned that the residual curvatures (κ_y^1 and κ_x^4) of the two stable states are determined by κ_y^0 and κ_x^3 .

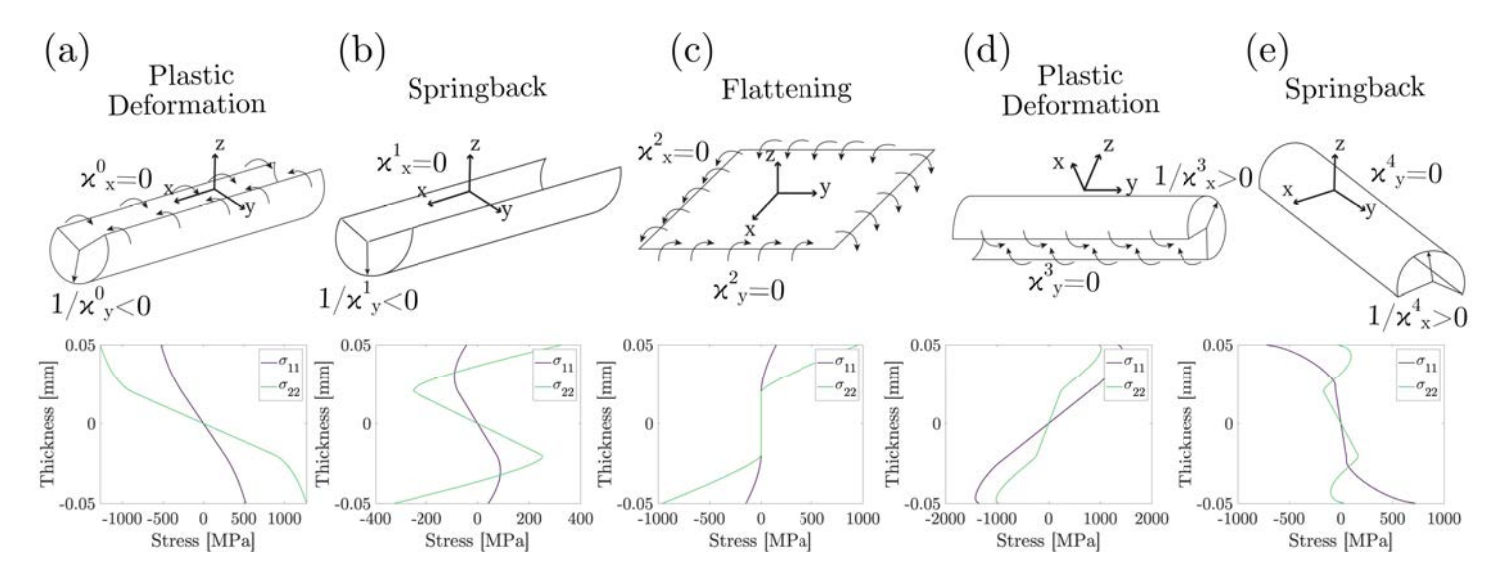


Figure A.1: Forming process for bistable isotropic laminates using plastic deformation. (a) \rightarrow (e) The sequential order of the forming process and the stress along the thickness at every step. (b) and (e) show the two stable states of the laminate.

For this procedure, we considered isotropic and kinematic hardening as shown in Ref. [65]. The final residual stress along the thickness of the laminate is calculated and utilized as an input for our FE simulations. To reduce computational time and avoid the numerical simulation of material plasticity, a thermal analogy is implemented to impose the residual stress as a thermally induced stress. We achieve this by calculating different thermal coefficients along the thickness of the laminate $(\alpha_{xx}^i, \alpha_{yy}^i)$ and fixing a temperature change $(\Delta T = 20)$. The thermal coefficients can be calculated using the following constitutive coefficients:

$$\alpha_{xx}^{i} = \frac{1}{E\Delta T} \left(\nu \sigma_{yy}^{i} - \sigma_{xx}^{i} \right), \tag{A.1a}$$

$$\alpha_{yy}^{i} = \frac{1}{E\Delta T} \left(\nu \sigma_{xx}^{i} - \sigma_{yy}^{i} \right), \tag{A.1b}$$

where index i represents one point in the thickness of the laminate, ΔT and E are constants through the simulation. By using this, we can get the two stable configurations described above.

Appendix B. Rayleigh-Ritz approach for finding stable states

A Rayleigh-Ritz approach is employed to minimize the total potential energy of a rectangular composite laminate to obtain its stable configurations, similar to the procedure outlined in Ref. [23]. The laminate has two sections: a prestress-free transition zone and a prestressed zone, as discussed in Sec. 5. The transition region has a $[0_2]_T$ layup, which results in a zero thermal prestress owing to its symmetry along the thickness direction. The prestressed zone has an unsymmetric $[90/0]_T$ layup and exhibits a prestress-induced curvature post-curing. The transition and the prestressed regions span $S1: x \in [0, L_s], y \in [-L_y/2, L_y/2]$ and $S2: x \in [L_s, L_x], y \in [-L_y/2, L_y/2]$ respectively. The displacement fields of the laminate are formulated as follows:

$$u^{i}(x,y) = \sum_{q=1}^{5} \sum_{r=1}^{5} \hat{c}_{uqr}^{i} x^{q} y^{r},$$
 (B.1a)

$$v^{i}(x,y) = \sum_{q=1}^{5} \sum_{r=1}^{5} \hat{c}_{vqr}^{i} x^{q} y^{r},$$
 (B.1b)

$$w^{i}(x,y) = \sum_{q=1}^{4} \sum_{r=1}^{4} \hat{c}_{wqr}^{i} x^{q} y^{r},$$
(B.1c)

where i = 1 for S1, i = 2 for S2. To avoid ill-conditioned terms in the strain energy function, normalized generalized coordinates are used. They are defined in terms of the generalized coordinates c_{pqr}^i as shown below:

$$\hat{c}_{pqr}^i = \frac{c_{pqr}^i}{L_x^q L_y^r},\tag{B.2}$$

where subscript p indicates the u, v or w displacement field, and q and r refer to the polynomial powers in x and y respectively. These polynomial shape functions are chosen based on previous research [8, 66] to accurately predict both the stable states of the laminate, with and without clamping the x = 0 edge. The fixed BC and continuity conditions imposed on the displacement fields are shown in Table B.1. These constraints eliminate some of the generalized coordinates in the analytical formulation, thereby reducing the number of degrees of freedom (DOFs) of the system. The mid-plane strains and curvatures are given by the von Kármán approximations while accounting for geometric nonlinearities in the strain-displacement relations:

$$\boldsymbol{\varepsilon_{i}^{0}} = \left[\varepsilon_{xx}^{0}, \ \varepsilon_{yy}^{0}, \ 2\varepsilon_{xy}^{0} \right]_{i} = \left[\frac{\partial u^{i}}{\partial x} + \frac{1}{2} \left(\frac{\partial w^{i}}{\partial x} \right)^{2}, \ \frac{\partial v^{i}}{\partial y} + \frac{1}{2} \left(\frac{\partial w^{i}}{\partial y} \right)^{2}, \ \frac{\partial u^{i}}{\partial y} + \frac{\partial v^{i}}{\partial x} + \frac{\partial w^{i}}{\partial x} \frac{\partial w^{i}}{\partial y} \right], \tag{B.3a}$$

$$\boldsymbol{\kappa_i^0} = \left[\kappa_{xx}^0, \ \kappa_{yy}^0, \ \kappa_{xy}^0\right]_i = \left[-\frac{\partial^2 w^i}{\partial x^2}, \ -\frac{\partial^2 w^i}{\partial y^2}, \ -2\frac{\partial^2 w^i}{\partial x \partial y}\right]. \tag{B.3b}$$

Table B.1: Fixed boundary conditions and continuity conditions used in the analytical formulation.

Fixed BC in section S1 at x = 0 Continuity between sections S1 and S2 at $x = L_s$

$$u^{1}(0,y) = 0$$

$$v^{1}(0,y) = 0$$

$$v^{1}(L_{s},y) = v^{2}(L_{s},y)$$

$$v^{1}(0,y) = 0$$

$$v^{1}(L_{s},y) = v^{2}(L_{s},y)$$

$$w^{1}(L_{s},y) = w^{2}(L_{s},y)$$

$$\frac{\partial w^{1}}{\partial x}(0,y) = 0$$

$$\frac{\partial w^{1}}{\partial x}(L_{s},y) = \frac{\partial w^{2}}{\partial x}(L_{s},y)$$

$$\frac{\partial w^{1}}{\partial y}(L_{s},y) = \frac{\partial w^{2}}{\partial y}(L_{s},y)$$

The strains as a function of the thickness location, z, are then found according to the Kirchhoff hypothesis:

$$\boldsymbol{\varepsilon_i} = \boldsymbol{\varepsilon_i^0} + z \boldsymbol{\kappa_i^0}. \tag{B.4}$$

It must be noted that the strain and curvature formulations shown here are different than the ones used in the extensible model presented in Sec. 3 because of different underlying assumptions. The laminate strain energy is the sum of the strain energies of both its sections. The strain energy of both sections is derived based on the Classical Lamination Theory (CLT) as follows:

$$\bar{U} = \sum_{i=1}^{2} \bar{U}_{i} = \sum_{i=1}^{2} \int_{L_{x}^{i}} \int_{L_{y}^{i}} \left(\frac{1}{2} \begin{bmatrix} \boldsymbol{\varepsilon}^{0} \\ \boldsymbol{\kappa}^{0} \end{bmatrix}_{i}^{'} \begin{bmatrix} \mathbb{A} & \mathbb{B} \\ \mathbb{B} & \mathbb{D} \end{bmatrix}_{i} - \begin{bmatrix} \boldsymbol{N_{T}} \\ \boldsymbol{M_{T}} \end{bmatrix}^{'} \right) \begin{bmatrix} \boldsymbol{\varepsilon}^{0} \\ \boldsymbol{\kappa}^{0} \end{bmatrix}_{i},$$
(B.5)

where \mathbb{A} , \mathbb{B} , and \mathbb{D} are the extension, extension-bending coupling, and bending stiffness matrices respectively. L_x^i and L_y^i are the domains of integration of each section in the x and y directions respectively. N_T and M_T refer to the stress and moment resultants due to a thermal prestress arising due to temperature change. The total potential energy of the laminate is calculated as:

$$U_{lam} = \bar{U} - W_{ext}. \tag{B.6}$$

The stable states of the laminate are found by minimizing U_{lam} with respect to the generalized coordinates:

$$\frac{\partial U_{lam}}{\partial c_{pqr}^i} = 0. ag{B.7}$$

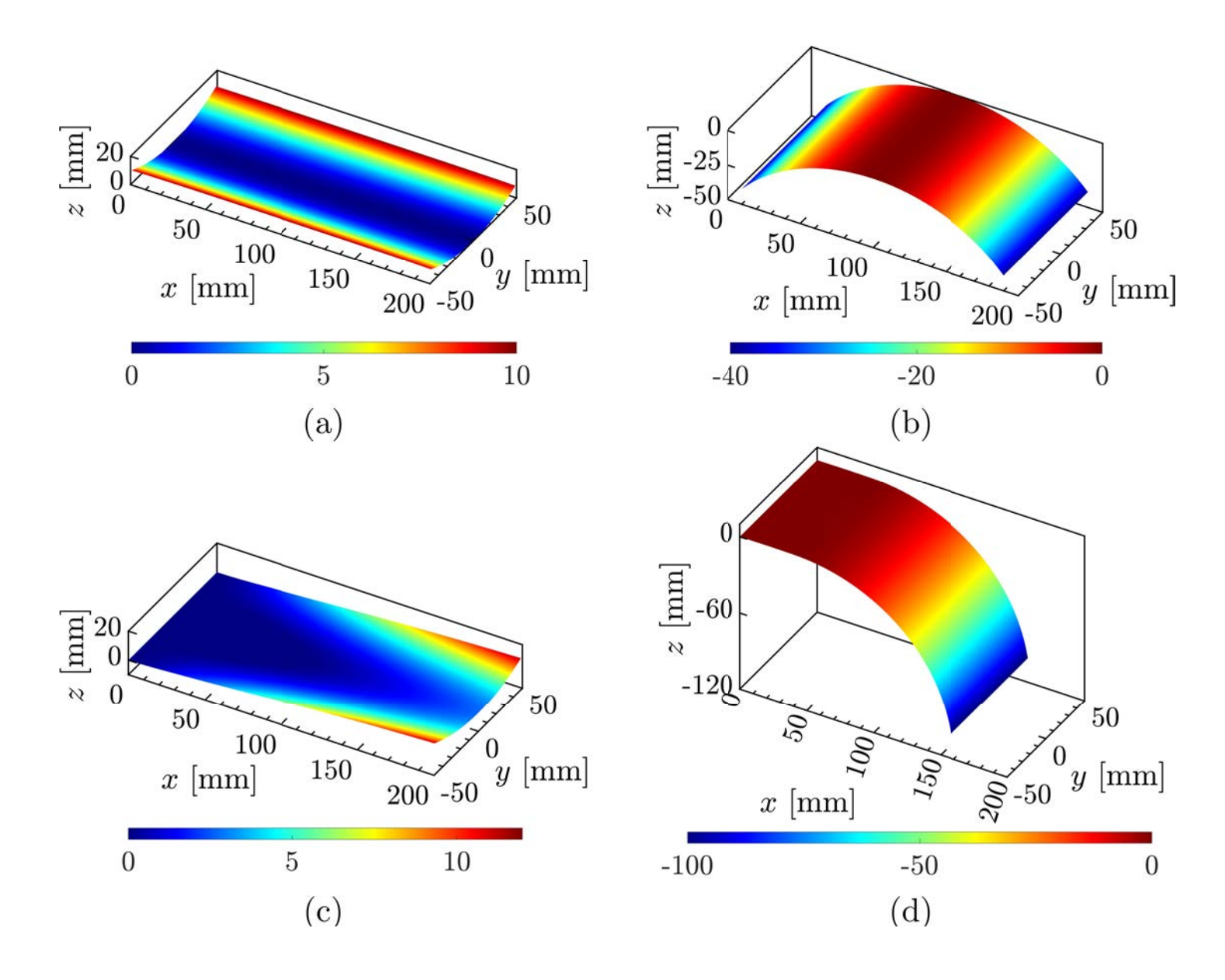


Figure B.1: (a) Stable state 1 and (b) state 2 of a free-free laminate (AR = 2, TR = 0) and (c), (d) States 1 and 2 of a fixed-free laminate (AR = 2, TR = 0.2) solved using the Rayleigh-Ritz minimization of the total potential energy.

The stability of the minima obtained is checked by assessing the positive definiteness of the Hessian matrix. Figures B.1a and B.1b show the two stable states of a single section 200 mm ×100 mm laminate with a $[90/0]_T$ layup and no clamped BC. In this case, the prestress-free transition zone is not included, thus making $L_s = 0$. Note that without this transition region, the laminate only has one section, and the boundary conditions shown in Table B.1 are imposed on S2 instead of S1. Since there is no external load applied on the laminate, $W_{ext} = 0$ in Eq. (B.6). Some of the generalized coordinates in Eq. (B.1) are eliminated by imposing symmetry about the y axis, and some terms that increase the computational cost without improving the accuracy are also excluded after repeated testing. The "FindMinimum" sub-

routine in Mathematica is employed to find the local minima of the total potential energy function. The displacements in both states found using the semi-analytical model are very similar to those observed in ABAQUS® simulations (see Fig. 2a). Similarly, the stable states of a clamped-free two-section laminate predicted by the Rayleigh-Ritz formulation are shown in Figures B.1c and B.1d, illustrating the bistability recovery in the presence of a prestress-free transition region. This analytical formulation can be useful to obtain the transverse radius of curvature of state 1, R, in the free-free configuration for use in the extensible model presented in Sec. 3. Also, the residual bending moments in this state due to prestress can be calculated using this approach by first calculating the in-plane stresses from the strains and integrating them along the thickness direction as follows:

$$M_{xx}^{ps} = \int_{-t/2}^{t/2} \sigma_{xx} z \ dz,$$
 (B.8a)

$$M_{yy}^{ps} = \int_{-t/2}^{t/2} \sigma_{yy} z \ dz.$$
 (B.8b)

Appendix C. Supplementary data

Supplementary data associated with this article has been submitted in addition to this manuscript.

References

- [1] Hyer MW. Some observations on the cured shape of thin unsymmetric laminates. J Compos Mater 1981;15(2):175-94. URL: https://doi.org/10.1177/002199838101500207.
- [2] Dano ML, Hyer MW. Thermally-induced deformation behavior of unsymmetric laminates. Int J Solids Struct 1998;35(17):2101–20. URL: https://doi.org/10.1016/S0020-7683(97)00167-4.
- [3] Dano ML, Hyer M. Snap-through of unsymmetric fiber-reinforced composite laminates. Int J Solids Struct 2002;39(1):175–98. URL: https://doi.org/10.1016/S0020-7683(01)00074-9.
- [4] Dano ML, Hyer M. SMA-induced snap-through of unsymmetric fiber-reinforced composite laminates. Int J Solids Struct 2003;40(22):5949–72. URL: https://doi.org/10.1016/S0020-7683(03) 00374-3.
- [5] Daynes S, Nall S, Weaver P, Potter K, Margaris P, Mellor P. On a bistable flap for an airfoil. In: 50th AIAA/ASME/ASCE/AHS/ASC Structures, Structural Dynamics, and Materials Conference. Structures, Structural Dynamics, and Materials and Co-located Conferences; American Institute of Aeronautics and Astronautics; 2009, URL: https://doi.org/10.2514/6.2009-2103.
- [6] Nicassio F, Scarselli G, Pinto F, Ciampa F, Iervolino O, Meo M. Low energy actuation technique of bistable composites for aircraft morphing. Aerosp Sci Technol 2018;75:35-46. URL: https://doi. org/10.1016/j.ast.2017.12.040.

- [7] Arrieta AF, Bilgen O, Friswell M, Hagedorn P. Dynamic control for morphing of bi-stable composites. J Intell Mater Syst Struct 2013;24:266–73. URL: https://doi.org/10.1177/1045389X12449918.
- [8] Udani JP, Arrieta AF. Analytical modeling of multi-sectioned bi-stable composites: Stiffness variability and embeddability. Compos Struct 2019;216:228–39. URL: https://doi.org/10.1016/j.compstruct.2019.02.015.
- [9] Hyer MW. Calculations of the room-temperature shapes of unsymmetric laminatestwo. J Compos Mater 1981;15(4):296-310. URL: https://doi.org/10.1177/002199838101500401.
- [10] Hyer MW. The room-temperature shapes of four-layer unsymmetric cross-ply laminates. J Compos Mater 1982;16(4):318-40. URL: https://doi.org/10.1177/002199838201600406.
- [11] Jun WJ, Hong CS. Cured shape of unsymmetric laminates with arbitrary lay-up angles. J Reinf Plast Compos 1992;11(12):1352–66. URL: https://doi.org/10.1177/073168449201101202.
- [12] Peeters LJB, Powell PC, Warnet L. Thermally-induced shapes of unsymmetric laminates. J Compos Mater 1996;30(5):603-26. URL: https://doi.org/10.1177/002199839603000504.
- [13] Iqbal K, Pellegrino S. Bi-stable composite shells. In: 41st Structures, Structural Dynamics, and Materials Conference and Exhibit. American Institute of Aeronautics and Astronautics; 2000, URL: https://doi.org/10.2514/6.2000-1385.
- [14] Iqbal K, Pellegrino S, Daton-Lovett A. Bi-stable composite slit tubes. In: Pellegrino S, Guest SD, editors. IUTAM-IASS Symposium on Deployable Structures: Theory and Applications. Dordrecht: Springer Netherlands. ISBN 978-94-015-9514-8; 2000, p. 153-62.
- [15] Galletly DA, Guest SD. Bistable composite slit tubes. I. A beam model. Int J Solids Struct 2004;41(16):4517-33. URL: https://doi.org/10.1016/j.ijsolstr.2004.02.036.
- [16] Knott G, Viquerat A. Helical bistable composite slit tubes. Compos Struct 2019;207:711-26. URL: https://doi.org/10.1016/j.compstruct.2018.09.045.
- [17] Murphey T, Pellegrino S. A novel actuated composite tape-Spring for deployable structures. In: 45th AIAA/ASME/ASCE/AHS/ASC Structures, Structural Dynamics, and Materials Conference and Exhibit. American Institute of Aeronautics and Astronautics; 2004,URL: https://doi.org/10.2514/6.2004-1528.
- [18] Wang B, Seffen K, Guest S. Folding of bistable composite tape-springs. 2019. doi:10.17863/CAM. 36403.
- [19] Xu B, Wang B, Fancey KS, Zhong S, Zhao C, Chen X. A bistable helical structure based on composite tape-springs. Compos Commun 2023;43:101723. URL: https://doi.org/10.1016/j.coco.2023.101723.
- [20] Liu TW, Bai JB, Wang ZZ, Fantuzzi N. Determining folded stable state of bistable deployable composite boom: An improved two-parameter analytical model. Acta Astronaut 2023;213:507–15. URL: https://doi.org/10.1016/j.actaastro.2023.09.018.

- [21] Liu TW, Bai JB, Xi HT, Fantuzzi N, Bu GY, Shi Y. Experimental and numerical investigation on folding stable state of bistable deployable composite boom. Compos Struct 2023;320:117178. URL: https://doi.org/10.1016/j.compstruct.2023.117178.
- [22] Bai JB, You FY, Wang ZZ, Fantuzzi N, Liu Q, Xi HT, et al. An efficient multi-objective optimization framework for thin-walled tubular deployable composite boom. Compos Struct 2024;327:117713. URL: https://doi.org/10.1016/j.compstruct.2023.117713.
- [23] Mattioni F. Thermally induced multi-stable composites for morphing aircraft applications. Ph.D. thesis; University of Bristol; 2009.
- [24] Pirrera A, Avitabile D, Weaver P. Bistable plates for morphing structures: A refined analytical approach with high-order polynomials. Int J Solids Struct 2010;47(25):3412-25. URL: https://doi.org/10.1016/j.ijsolstr.2010.08.019.
- [25] Lamacchia E, Pirrera A, Chenchiah IV, Weaver PM. Morphing shell structures: A generalised modelling approach. Compos Struct 2015;131:1017–27. URL: https://doi.org/10.1016/j.compstruct. 2015.06.051.
- [26] Nicassio F. Shape prediction of bistable plates based on Timoshenko and Ashwell theories. Compos Struct 2021;265:113645. URL: https://doi.org/10.1016/j.compstruct.2021.113645.
- [27] Guest S, Pellegrino S. Analytical models for bistable cylindrical shells. Proc R Soc A Math Phys Eng Sci 2006;462(2067):839–54. URL: https://doi.org/10.1098/rspa.2005.1598.
- [28] Zhang Z, Wu H, He X, Wu H, Bao Y, Chai G. The bistable behaviors of carbon-fiber/epoxy antisymmetric composite shells. Compos B Eng 2013;47:190-9. URL: https://doi.org/10.1016/j.compositesb.2012.10.040.
- [29] Yang L, Tan H, Cao Z. Modeling and analysis of the ploy region of bistable composite cylindrical shells. Compos Struct 2018;192:347–54. URL: https://doi.org/10.1016/j.compstruct.2018.02.085.
- [30] Li H, Dai F, Weaver P, Du S. Bistable hybrid symmetric laminates. Compos Struct 2014;116:782–92. doi:https://doi.org/10.1016/j.compstruct.2014.05.030.
- [31] Anilkumar PM, Haldar A, Jansen E, Rao BN, Rolfes R. Design optimization of multistable variable-stiffness laminates. Mech Adv Mater Struct 2019;26(1):48–55. doi:https://doi.org/10.1080/15376494.2018.1512022.
- [32] Haldar A, Groh R, Jansen E, Weaver PM, Rolfes R. An efficient semi-analytical framework to tailor snap-through loads in bistable variable stiffness laminates. Int J Solids Struct 2020;195:91–107. doi:https://doi.org/10.1016/j.ijsolstr.2020.02.018.
- [33] Zhang Z, Pei K, Sun M, Wu H, Wu H, Jiang S, et al. Tessellated multistable structures integrated with new transition elements and antisymmetric laminates. Thin Wall Struct 2022;170:108560. doi:https://doi.org/10.1016/j.tws.2021.108560.

- [34] Arrieta AF, Kuder IK, Waeber T, Ermanni P. Variable stiffness characteristics of embeddable multi-stable composites. Compos Sci Technol 2014;97:12-8. URL: https://doi.org/10.1016/j.compscitech.2014.03.017.
- [35] Emam SA, Inman DJ. A review on bistable composite laminates for morphing and energy harvesting. Appl Mech Rev 2015;67(060803). URL: https://doi.org/10.1115/1.4032037.
- [36] Scarselli G, Nicassio F, Maffezzoli A. Mechanical characterization of bistable laminates for very small aircraft morphing applications. In: Health Monitoring of Structural and Biological Systems XII; vol. 10600. SPIE; 2018, p. 415–24. URL: https://doi.org/10.1117/12.2300194.
- [37] Brunetti M, Favata A, Vidoli S. Enhanced models for the nonlinear bending of planar rods: localization phenomena and multistability. Proc R Soc A Math Phys Eng Sci 2020;476. URL: https://doi.org/10.1098/rspa.2020.0455.
- [38] Seffen K, Wang B, Guest S. Folded orthotropic tape-springs. J Mech Phys Solids 2019;123:138–48. URL: https://doi.org/10.1016/j.jmps.2018.09.017.
- [39] Phatak S, Myers OJ, Li S, Fadel G. Defining relationships between geometry and behavior of bistable composite laminates. J Compos Mater 2021;55(22):3049–59. doi:10.1177/00219983211005824.
- [40] Betts DN, Kim HA, Bowen CR. Optimization of stiffness characteristics for the design of bistable composite laminates. AIAA J 2012;50(10):2211–8. doi:10.2514/1.J051535.
- [41] Arrieta AF, Bilgen O, Friswell M, Ermmani P. Modelling and configuration control of wing-shaped bi-stable piezoelectric composites under aerodynamic loads. Aerosp Sci Technol 2013;29:453–61. URL: https://doi.org/10.1016/j.ast.2013.05.004.
- [42] Bilgen O, Arrieta AF, Friswell M, Hagedorn P. Dynamic control of a bistable wing under aerodynamic loading. Smart Mater Struct 2013;22:025020. URL: https://doi.org/10.1088/0964-1726/22/2/ 025020.
- [43] Arrieta AF, Bilgen O, Friswell M, Hagedorn P. Passive load alleviation bi-stable morphing concept. AIP Adv 2012;2. URL: https://doi.org/10.1063/1.4739412.
- [44] Arrieta AF, Kuder IK, Rist M, Waeber T, Ermanni P. Passive load alleviation aerofoil concept with variable stiffness multi-stable composites. Compos Struct 2014;116:235–242. URL: https://doi.org/10.1016/j.compstruct.2014.05.016.
- [45] Kuder IK, Arrieta AF, Rist M, Ermanni P. Aeroelastic response of a selectively compliant morphing aerofoil featuring integrated variable stiffness bi-stable laminates. J Intell Mater Syst Struct 2016;27(14):1949–66. URL: https://doi.org/10.1177/1045389X15620038.
- [46] Boddapati K, Arrieta AF. Design of bistable laminates with low aspect ratio. In: Smart Materials, Adaptive Structures and Intelligent Systems; vol. 85499. American Society of Mechanical Engineers; 2021, p. V001T05A017. URL: https://doi.org/10.1115/SMASIS2021-68285.

- [47] Boddapati K, Boston DM, Rivas-Padilla JR, Arrieta AF. Aero-structural response of a slitted bistable laminate. In: Smart Materials, Adaptive Structures and Intelligent Systems; vol. 87523. American Society of Mechanical Engineers; 2023, p. V001T04A004. URL: https://doi.org/10.1115/ SMASIS2023-110581.
- [48] Sanders B, Eastep FE, Forster E. Aerodynamic and aeroelastic characteristics of wings with conformal control surfaces for morphing aircraft. J Aircr 2003;40(1):94–9. URL: https://doi.org/10.2514/2.3062.
- [49] Schioler T, Pellegrino S. A bistable structural element. Proc Inst Mech Eng C J Mech Eng Sci 2008;222(11):2045-51. URL: https://doi.org/10.1243/09544062JMES982.
- [50] Brunetti M, Vidoli S, Vincenti A. Bistability of orthotropic shells with clamped boundary conditions: An analysis by the polar method. Compos Struct 2018;194:388-97. URL: https://doi.org/10.1016/j.compstruct.2018.04.009.
- [51] Brunetti M, Vincenti A, Vidoli S. A class of morphing shell structures satisfying clamped boundary conditions. Int J Solids Struct 2016;82:47-55. URL: https://doi.org/10.1016/j.ijsolstr.2015. 12.017.
- [52] Barois T, Tadrist L, Quilliet C, Forterre Y. How a curved elastic strip opens. Phys Rev Lett 2014;113(21):214301. URL: https://doi.org/10.1103/PhysRevLett.113.214301.
- [53] Wang B, Seffen K, Guest S. Folded strains of a bistable composite tape-spring. Int J Solids Struct 2021;URL: https://doi.org/10.1016/j.ijsolstr.2021.111221.
- [54] Horgan C, Simmonds J. Saint-Venant end effects in composite structures. Compos Eng 1994;4(3):279–86. URL: https://doi.org/10.1016/0961-9526(94)90078-7.
- [55] Horgan CO, Carlsson LA. Saint-Venant end effects for anisotropic materials. In: Beaumont PW, Zweben CH, editors. Comprehensive Composite Materials II. Oxford: Elsevier. ISBN 978-0-08-100534-7; 2018, p. 38–55. URL: https://doi.org/10.1016/B0-08-042993-9/00034-6.
- [56] Smith M. ABAQUS/Standard User's Manual, Version 6.9. United States: Dassault Systemes Simulia Corp.; 2009.
- [57] Tawfik S, Tan X, Ozbay S, Armanios E. Anticlastic stability modeling for cross-ply composites. J Compos Mater 2007;41(11):1325–38. URL: https://doi.org/10.1177/0021998306068073.
- [58] Betts DN, Salo AI, Bowen CR, Kim HA. Characterisation and modelling of the cured shapes of arbitrary layup bistable composite laminates. Compos Struct 2010;92(7):1694-700. URL: https://doi.org/10.1016/j.compstruct.2009.12.005.
- [59] Mattioni F, Weaver P, Friswell M. Multistable composite plates with piecewise variation of lay-up in the planform. Int J Solids Struct 2009;46(1):151-64. URL: https://doi.org/10.1016/j.ijsolstr. 2008.08.023.

- [60] Qatu MS, Sullivan RW, Wang W. Recent research advances on the dynamic analysis of composite shells: 2000–2009. Compos Struct 2010;93(1):14–31. URL: https://doi.org/10.1016/j.compstruct.2010.05.014.
- [61] Lee JG, Ryu J, Kim SW, Koh JS, Cho KJ, Cho M. Effect of initial tool-plate curvature on snapthrough load of unsymmetric laminated cross-ply bistable composites. Compos Struct 2015;122:82-91. URL: https://doi.org/10.1016/j.compstruct.2014.11.037.
- [62] Kollar LP, Springer GS. Mechanics of composite structures. Cambridge university press; 2003.
- [63] Bert CW. Classical lamination theory. In: Manual on experimental methods for mechanical testing of composites. Springer; 1989, p. 11–6.
- [64] Calladine CR. Theory of shell structures. Cambridge university press; 1983.
- [65] Kebadze E, Guest S, Pellegrino S. Bistable prestressed shell structures. Int J Solids Struct 2004;41(11-12):2801-20. URL: https://doi.org/10.1016/j.ijsolstr.2004.01.028.
- [66] Schultz MR, Hyer MW, Brett Williams R, Keats Wilkie W, Inman DJ. Snap-through of unsymmetric laminates using piezocomposite actuators. Compos Sci Technol 2006;66(14):2442-8. URL: https://doi.org/10.1016/j.compscitech.2006.01.027; special Issue in Honour of Professor C.T. Sun.